Finite element modelling of traction-free cracks: Benchmarking the augmented finite element method (AFEM)

Simon Essongue, Guillaume Couégnat, Eric Martin

Finite element modelling of traction-free cracks: Benchmarking the augmented finite element method (AFEM)

Simon Essongue[a,*], Guillaume Couégnat[b], Eric Martin[b]

[a] *Institut Clément Ader, Université de Toulouse, CNRS-INSA-ISAE-Mines Albi-UPS, 3 Rue Caroline Aigle, 31400 Toulouse, France*
[b] *Laboratoire des Composites Thermostructuraux, UMR5801 CNRS/Univ. Bordeaux/Safran/CEA, 3 Allée de la Boétie, 33600 Pessac, France*

Abstract

This paper investigates the accuracy and the convergence properties of the augmented finite element method (AFEM). The AFEM is here used to model strong discontinuities independently of the underlying mesh. One noticeable advantage of the AFEM over other partition of unity methods is that it does not introduce additional global unknowns to represent cracks. Numerical 2D experiments illustrate the performance of the method and draw comparisons with the element deletion method (EDM), the phantom node method (PNM), the finite element method (FEM) and the embedded finite element method (EFEM). The h-convergence in the energy norm of the AFEM is studied for the first time and it is shown to outperform the aforementioned numerical methods when cracks are loaded in Mode I.

Key words: embedded discontinuities, embedded finite elements, strong discontinuities, augmented finite element method, phantom node method

1. INTRODUCTION

The finite element method (FEM) has become a classical tool to design and analyse engineering structures. To predict structural failure scenarios, the nucleation and propagation of cracks have to be explicitly considered. The use of standard finite elements can then become prohibitive since remeshing is needed as cracks grow. Moreover, the number of degrees of freedom (DOF) may drastically increase, especially in three-dimensional applications, and projecting the solution on the updated mesh is costly besides potentially degrading the quality of results [1]. Thus, it seems desirable to take another road for the modelling of multiple crack propagation in structures.

To ease analysis involving cracks, numerous variants of the FEM allowing embedded cracks within elements have been developed. These variants, usually gathered as "enriched finite element methods" [2, 3], encompass a wide variety of methods such as the extended finite element method (XFEM) [4], the generalized finite element method (GFEM) [5], the phantom node method (PNM) [6], the cut finite element method (CutFEM) [7] or the embedded finite element method (EFEM) [8], to name a few.

These methods exhibit numerous differences, but, the most striking one is that EFEMs can model an arbitrary number of (possibly growing) cracks without increasing the number of DOF per element, or the size of the assembled stiffness matrix. Yet, this attractive property, not shared by any of the aforementioned methods, comes at a price: the interelement compatibility of the displacement field is lost (see Figure 1).

*Corresponding author
Email address: simon.essongue-boussougou@isae-supaero.fr (Simon Essongue)

Nomenclature

$[B^+]$, $[B^-]$ Strain-displacement matrices of the upper and lower subdomains, respectively

$\boldsymbol{C}^+$, $\boldsymbol{C}^-$ Stiffness tensors of the upper and lower subdomains, respectively

$\{d^+\}$, $\{d^-\}$ Vectors of degrees of freedom of the upper and lower subdomains

$\{dext^+\}$, $\{dext^-\}$ Vectors of external nodal displacements of subdomains Ω^+ and Ω^+

$\{dint^+\}$, $\{dint^-\}$ Vectors of nodal displacements related to surfaces Γ_c^+ and Γ_c^-

$\mathbf{e}$ Error measure

E Young's modulus

$\{fcohesive^+\}$, $\{fcohesive^-\}$ Vectors of nodal cohesive forces applied on Γ_c^+ and Γ_c^-

$\{fext^+\}$, $\{fext^-\}$ Vectors of nodal external forces applied on the upper and lower subdomains

$\mathcal{G}$ Energy release rate

K_1, K_2 Mode I and Mode II stress intensity factors

$[L^+]$, $[L^-]$ Stiffness matrices of the upper and lower subdomains

$[L_{ij}^+]$, $[L_{ij}^-]$ Submatrices of $[L^+]$ and $[L^-]$

$\mathbf{n}^+$, $\mathbf{n}^-$ Outward pointing normals of Ω^+ and Ω^-

$[N^+]$, $[N^-]$ Shape function matrices that interpolate the displacement field in Ω^+ and Ω^-

q_1 Weight function

$\mathbf{t}_{\mathbf{ext}}^+$, $\mathbf{t}_{\mathbf{ext}}^-$ External tractions applied on the upper and lower subdomains

$\mathbf{t}_{\mathbf{int}}^+$, $\mathbf{t}_{\mathbf{int}}^-$ Tractions along the discontinuity surfaces Γ_c^+ and Γ_c^-

$\mathbf{u}^+$, $\mathbf{u}^-$ Displacement field in the upper and lower subdomains

$\bar{\mathbf{u}}^+$, $\bar{\mathbf{u}}^-$ Imposed displacement in the upper and lower subdomains

W Strain energy density

Γ_c Domain occupied by the crack surface

Γ_c^+, Γ_c^- Crack surfaces in the upper and lower subdomains

δ_{ij} Kronecker delta function

$\boldsymbol{\epsilon}^+$, $\boldsymbol{\epsilon}^-$ Strain field in the upper and lower subdomains

$\boldsymbol{\eta}$ Relative error measure

ν Poisson's ratio

$\boldsymbol{\sigma}^+$, $\boldsymbol{\sigma}^-$ Stress field in the upper and lower subdomains

Ω Volume occupied by the cracked solid

Ω^+, Ω^- Domains occupied by the upper and lower subdomains

AFEM Augmented Finite Element Method

AQ4-TIP, AQ4 4-node Augmented Quadrilateral element with and without crack-tip treatment

AQ4-1 4-node Augmented Quadrilateral element made of two quadrilateral subdomains

AQ4-2 4-node Augmented Quadrilateral element made of a triangular and a pentagonal subdomains

AT3-TIP, AT3 3-node Augmented Triangular element with and without crack-tip treatment

CutFEM Cut Finite Element Method

DOF Degrees Of Freedom

EDM Element Deletion Method

EFEM Embedded Finite Element Method

EFEM-SM Embedded Finite Element Method with enhanced Strain Modes

FEM Finite Element Method

GFEM Generalized Finite Element Method

IP Integration Point

PNM Phantom Node Method

P5 5-node Pentagonal finite element

Q4 4-node Quadrilateral finite element

SIF Stress Intensity Factor

SKON Statically and Kinematically Optimal Nonsymmetric Formulation

T3 3-node Triangular finite element

XFEM eXtended Finite Element Method

Despite this drawback, some EFEMs have been reported to be more "coarse mesh accurate" than well-established methods such as the XFEM [9, 10]. Even though EFEMs possess numerous desirable properties, they are scarcely used compared to the other aforesaid methods. One reason probably stems from the numerous variants that have been published so far, moreover, they are still undergoing significant evolutions, see, *e.g.*, [11–13]. The most recent

EFEMs have never been compared and their performance and convergence rates are little known. Hence, although EFEMs have proven to be valuable tools with a broad scope of application, key information is still missing to widen their acceptance and use, and it remains unclear how to decide which EFEM is best suited to solve a given problem, or how it compares with other EFEM variants.

The goal of this study is to narrow this knowledge gap. To do so, quantitative estimates of the convergence rates and accuracy of various EFEMs must be made available. Previous EFEMs studies mainly focused on the convergence of local quantities of interest, such as reaction forces, but, when a deeper understanding or assessment is sought, more advanced measures are also needed[14]. This is in sharp contrast with methods such as the XFEM, whose convergence has been proven [15], and convergence rates numerically checked[16, 17].

Our study will focus on the EFEM proposed by Yang and co-workers: the augmented finite element method[18, 19] (AFEM). These authors developed an EFEM whose formulation is straightforward and that departs from others EFEMs on several aspects: *i)* it allows to model weak discontinuities (*i.e.*, material interfaces) and strong discontinuities (*i.e.*, cracks) as well as the transition from the former to the latter, *ii)* it gives rise to symmetrical stiffness matrices, *iii)* it permits to embed multiple intersecting discontinuities within an element and *iv)* it does not require iterations at the element level, even if nonlinear cohesive cracks are employed[20]. The relative simplicity of the AFEM formulation allowed the authors to rapidly extend it to thermomechanical applications [21], dynamic loadings [22], three-dimensional studies of heterogeneous materials [23] as well as large deformation of shells [24]. The method has been implemented as a user element in Abaqus and is reported to be $\simeq 50$ times faster than the phantom node method (PNM) natively available in this software[20].

In the present work, we restricted ourselves to the modelling of traction-free cracks, thus omitting the use of cohesive zones. From their very inception, EFEMs were designed to model the propagation of cohesive cracks that cancel stress singularities and circumvent pathological mesh-dependency [25]. Nevertheless, much is to be gained from our "traction-free study" since we can rely on available analytical solutions and hence provide precise estimates of the accuracy and convergence properties of the AFEM in this situation. Such estimates would be notoriously more difficult to compute in the presence of cohesive cracks (see, *e.g.*, [14]). Our assessment of the AFEM accuracy includes: *i)* the study of locking properties, *ii)* the investigation of crack-induced stiffness losses in structures, *iii)* the h-convergence in the energy norm and *iv)* the accuracy of the estimated stress-intensity factors. Quantitative comparisons with the standard finite element method (FEM), the phantom node method (PNM), the element deletion method (EDM) and another embedded finite element method (EFEM) will also be drawn. In Section 2, the methods that will be compared with the AFEM in this study are presented. In Section 3, the derivation of the AFEM for the modelling of traction-free cracks is detailed. In Section 4, we consider several numerical tests to evaluate the performances of the AFEM and compare it to the other aforementioned methods.

2. MODELLING OF TRACTION-FREE CRACKS WITH SOME FINITE ELEMENT BASED METHODS

This section introduces the methods to be compared with the augmented finite element method (AFEM) throughout the paper: the element deletion method (EDM), the finite element method (FEM), the phantom node method (PNM) and the embedded finite element method (EFEM).

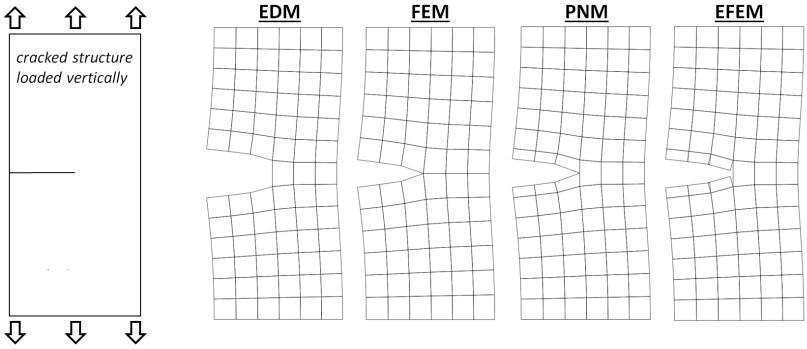

Figure 1: Modelling of a cracked solid with various numerical methods: the element deletion method (EDM), the finite element method (FEM), the phantom node method (PNM) and the embedded finite element method (EFEM)

2.1. The element deletion method (EDM)

The element deletion method (EDM), also called "kill element strategy", "element removal methodology" or "element erosion", is one of the earliest method employed to represent cracks with standard finite elements. Its application is straightforward since cracks are simply modelled by a set of deleted elements, see Figure 1. Although the method is called element deletion method, elements are not necessarily suppressed from the mesh, but their stresses are set to zero whatever the strain state. The EDM gives rise to cracked volumes, termed "blunt cracks" [26], instead of crack surfaces, denoted as "sharp cracks" or "discrete cracks" in the remainder of this work. One noteworthy application of the EDM is crash/impact simulations conducted with the so-called explicit finite element scheme (see, among others, [27]). Explicit schemes are conditionally stable and the stable time step decreases as the mesh gets distorted, (see, *e.g.*, chapter 4.5[27]). Thus, to get a solution in an acceptable amount of time, some authors erode the elements that reduce the stable time step below a user-defined value (see, *e.g.*, chapter 4.3[27]).

Several fracture mechanics related theories also involve the use of the EDM, in conjunction with the standard FEM: Eigenfracture [28], Continuum Damage Models[29], or Finite Fracture Mechanics [30] to name a few. To the best of the authors' knowledge, the accuracy at which sharp cracks can be modelled with the EDM has not been fully evaluated in the literature. The EDM was shown to give sufficiently accurate stress intensity factor to be considered for crack propagation analysis[26]. Yet, its convergence rate (*e.g.*, in the energy norm) remains unknown. In this study, the elements intersected by a crack are not deleted but their stress state is set to zero. The meshes are made of standard finite elements: either constant strain triangles integrated with a 1-point integration scheme or bilinear quadrilateral integrated with a 2×2 Gauss integration scheme. The formulation of standard finite elements is not recalled here and we refer the interested reader to reference textbooks[31–33].

2.2. The standard finite element method (FEM)

A straightforward manner to represent cracks, also called strong discontinuities[25], is to mesh them explicitly with the standard FEM, as depicted in Figure 1. It is one of the most employed technique to model strong discontinuities [34], and, contrary to the element deletion method, it allows to represent cracks as surfaces. When the simulation of growing cracks is undertaken, adaptative remeshing must be employed so that the mesh conforms to the evolving crack geometry. Continuously updating the mesh and computing quantities of interest (*e.g.*, stress intensity factors or

energy release rate) is a tedious task and sophisticated algorithms need to be employed[35]. Furthermore, the presence of cracks makes the stress field singular, which in turns degrades the convergence rate of the FEM. Indeed, problems comprising strong discontinuities converge with an error of $\mathcal{O}(h^{0.5})$ in the energy norm, independently of the order of the finite elements [36]. Moreover, special finite elements are often employed in the vicinity of the crack tip to accurately compute stress intensity factors see, *e.g.*, [37]. The FE meshes used in this study are either composed of linear triangular elements with one integration point or bilinear quadrilateral elements integrated with a 2×2 Gauss scheme.

2.3. The phantom node method (PNM)

To overcome the remeshing difficulties, enriched variants of the standard FEM that allow embedding cracks within elements have been developed. The most popular extensions include the extended finite element method (XFEM)[4], the generalized finite element method (GFEM) [5] and the phantom node method (PNM) [6]. These approaches are special instances of the partition of unity method (PUM) [15] and are now recognised to be closely related [38]. They are implemented in numerous commercial softwares (*e.g.*, SAMCEF, ABAQUS, LS-DYNA or ANSYS) and are used to solve problems of industrial complexity [2]. Their main drawback is that the discontinuities are modelled thanks to additional degrees of freedom located at the standard element nodes. Hence, as the cracks grow, the set of equations to be solved at the global level increases. The resulting dynamic allocation of degrees of freedom complicates the efficient implementation of these methods. The PNM, the GFEM, and the XFEM are closely related as the extrinsic enrichments used in these methods have the same structure. When employed to model traction-free cracks, they are of similar accuracy and share the same convergence rates [39]. As with the FEM, the convergence rate of these methods when modelling traction-free cracks is suboptimal. Indeed, unless a special geometrical enrichment [16, 17] is used in the vicinity of the crack tip, these methods converge with an error of $\mathcal{O}(h^{0.5})$ in the energy norm, whatever the order of the shape functions [17]. In this paper, we make use of the phantom node method natively integrated in the software ABAQUS v6.16. A noteworthy attribute of the PNM is that it is easier to implement than other enriched formulation such as the XFEM since cracks are somewhat modelled thanks to overlapping elements[38, 39]. The formulation of the phantom node method is not recalled here and we direct the interested reader to dedicated papers [6].

2.4. Embedded finite element method (EFEM) with enhanced strain modes (SM)

The development of embedded finite element methods, also called finite element methods with embedded discontinuities (EFEMs) [8], started in the early 90's [40]. They share the same purpose as the XFEM or the PNM: representing discontinuities independently of the mesh. To model cracks, EFEMs make use of element-supported enrichments, which strongly differs from the XFEM that employs node-supported enrichments [9]. As a result, the degrees of freedom that represent the EFEMs enrichments can be condensed at the element-level. The condensation process leads to interelement discontinuities in the displacement field, see Figure 1, but the resulting problem is not larger than the original one, no matter the number of discontinuities, which is a striking advantage when compared with the XFEM, the PNM or the GFEM. Despite their noteworthy convenience, EFEMs have not been incorporated into commercial codes yet, possibly due to the limitations inherent to early formulations of EFEMs. In the late 90's, Jirásek compared and classified the EFEMs published at that time [8]. He concluded that only three classes of EFEMs existed, and that one was superior to the others: the so-called statically and kinematically optimal nonsymmetric formulation (SKON).

He then used it to solve typical concrete fracture problems [41] and, although satisfactory results were obtained, some severe drawbacks were also noticed[42]. In the aforementioned reference, the authors demonstrated that the strains on both part of an embedded finite element split up by a crack are not fully decoupled, even after complete failure, leading to stress locking, *i.e.*, non-vanishing stress transfers across a fully opened discontinuity. They concluded that XFEM was preferable due its superior kinematic properties. Later EFEMs formulations aimed at overcoming these deficiencies. Their root causes lie in a poor kinematic description of the crack opening, as discovered in [43]. Indeed, a constant crack opening was usually adopted with early EFEMs and led to stress locking. The incorporation of non-uniform crack openings, also called hinge modes [43], non-uniform discontinuity modes [44], strain modes [45] or separation modes [46], proved to be a successful way to suppress locking. It was for instance demonstrated in [3] that the use of the SKON, equipped with enhanced strain mode, produces similar results as the XFEM. Hence, the use of EFEMs with non-uniform crack openings is a promising way to model discrete cracks without introducing additional degrees of freedom. Nevertheless, the design of the aforesaid strain modes is involved and, to the authors best knowledge, has been seldom performed in 3D or with high-order elements[47, 48]. In this paper, we will consider some of the results published by Linder and Armero, related to an EFEM equipped with enhanced strain modes[45]. Their EFEM will be denoted as "EFEM with Strain Modes" (EFEM-SM) in the remainder of this work. The formulation of this EFEM-SM is not presented here and we direct the interested reader to the aforesaid paper.

3. MODELLING OF TRACTION-FREE CRACKS WITH THE AUGMENTED FINITE ELEMENT METHOD (AFEM)

The augmented finite element method (AFEM), developed by Yang and co-workers[18], belongs to the category of embedded finite element methods (EFEMs). It departs from other EFEMs since it does not make use of enhanced strain modes and, yet, it is free from stress locking. Another noteworthy attribute of the AFEM is that it allows to model weak discontinuities (*i.e.*, material interfaces) and strong discontinuities, as well as the transition from the former to the latter. Moreover, it permits to embed multiple intersecting discontinuities within an element. The AFEM literature focuses on the modelling of cohesive cracks. In this document, we will however deal with traction-free cracks. The "traction-free crack derivation" of the AFEM that we are about to present must not be considered as another AFEM, but as a subset of the original one. Indeed, as soon as a cohesive crack is fully damaged and opened, the original AFEM and the "traction-free crack AFEM" are identical. The traction-free crack derivation allowed us to discover some key aspects of the AFEM while keeping the number of equations to a minimum.

3.1. Strong form, weak form and condensed discretized equilibrium equation

The reference situation to be considered is schematised in Figure 2. Let Ω be the domain occupied by a solid. A material point inside the domain is labelled as $\mathbf{x} \in \Omega$. A strong discontinuity surface $\Gamma_c = \Gamma_c^+ \cup \Gamma_c^-$ splits Ω into two subdomains Ω^+ and Ω^-. The prescribed external tractions $\mathbf{t}^+_{\mathbf{ext}}$ and $\mathbf{t}^-_{\mathbf{ext}}$ are applied on boundary $\Gamma_t = \Gamma_t^+ \cup \Gamma_t^-$ whereas the displacements $\bar{\mathbf{u}}^+$ and $\bar{\mathbf{u}}^-$ are imposed on boundary $\Gamma_u = \Gamma_u^+ \cup \Gamma_u^-$. The domains on both sides of the discontinuity are assumed to be elastic and homogeneous, yet Ω^+ and Ω^- can be made of different materials. We further assume small strain and displacement conditions. In the absence of body forces the field equations governing

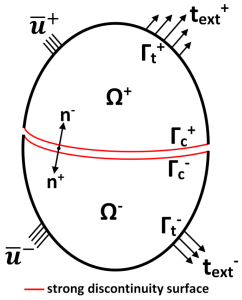

Figure 2: Solid body crossed by a strong discontinuity surface

the boundary value problem obey the following relations

$$\nabla\boldsymbol{\sigma}^+(\mathbf{x}) = \mathbf{0} \qquad \mathbf{x} \in \Omega^+ \qquad \nabla\boldsymbol{\sigma}^-(\mathbf{x}) = \mathbf{0} \qquad \mathbf{x} \in \Omega^- \tag{1}$$

$$\boldsymbol{\sigma}^+(\mathbf{x}).\mathbf{n}^+(\mathbf{x}) = \mathbf{t}^+_{\mathbf{ext}}(\mathbf{x}) \qquad \mathbf{x} \in \Gamma_t^+ \qquad \boldsymbol{\sigma}^-(\mathbf{x}).\mathbf{n}^-(\mathbf{x}) = \mathbf{t}^-_{\mathbf{ext}}(\mathbf{x}) \qquad \mathbf{x} \in \Gamma_t^- \tag{2}$$

$$\mathbf{u}^+(\mathbf{x}) = \bar{\mathbf{u}}^+(\mathbf{x}) \qquad \mathbf{x} \in \Gamma_u^+ \qquad \mathbf{u}^-(\mathbf{x}) = \bar{\mathbf{u}}^-(\mathbf{x}) \qquad \mathbf{x} \in \Gamma_u^- \tag{3}$$

$$\mathbf{t}^+_{\mathbf{int}}(\mathbf{x}) = \boldsymbol{\sigma}^+(\mathbf{x}).\mathbf{n}^+(\mathbf{x}) \qquad \mathbf{x} \in \Gamma_c^+ \qquad \mathbf{t}^-_{\mathbf{int}}(\mathbf{x}) = \boldsymbol{\sigma}^-(\mathbf{x}).\mathbf{n}^-(\mathbf{x}) \qquad \mathbf{x} \in \Gamma_c^- \tag{4}$$

$\boldsymbol{\sigma}^+$ and $\boldsymbol{\sigma}^-$ stand for the stress fields in Ω^+ and Ω^- respectively, $\mathbf{t}^+_{\mathbf{int}}$ and $\mathbf{t}^-_{\mathbf{int}}$ are the tractions along the discontinuity surfaces Γ_c^+ and Γ_c^- whereas $\mathbf{n}^+$ and $\mathbf{n}^-$ are the outward pointing normals of Ω^+ and Ω^- respectively. The constitutive law and the strain-displacement equations for the two subdomains read

$$\boldsymbol{\sigma}^+(\mathbf{x}) = \mathbf{C}^+ : \boldsymbol{\epsilon}^+(\mathbf{x}) \qquad \mathbf{x} \in \Omega^+ \qquad \boldsymbol{\epsilon}^+(\mathbf{x}) = \frac{1}{2}(\nabla^T\mathbf{u}^+(\mathbf{x}) + \nabla\mathbf{u}^+(\mathbf{x})) \qquad \mathbf{x} \in \Omega^+ \tag{5}$$

$$\boldsymbol{\sigma}^-(\mathbf{x}) = \mathbf{C}^- : \boldsymbol{\epsilon}^-(\mathbf{x}) \qquad \mathbf{x} \in \Omega^- \qquad \boldsymbol{\epsilon}^-(\mathbf{x}) = \frac{1}{2}(\nabla^T\mathbf{u}^-(\mathbf{x}) + \nabla\mathbf{u}^-(\mathbf{x})) \qquad \mathbf{x} \in \Omega^- \tag{6}$$

where $\mathbf{C}^+$ and $\mathbf{C}^-$ are the stiffness tensors of the subdomains Ω^+ and Ω^- respectively. The displacement fields $\mathbf{u}^+$ and $\mathbf{u}^-$ are subsets of the kinematically admissible displacement field, $\mathbf{U}$:

$$\mathbf{u}^+ \in \mathbf{U} = \{\mathbf{v}^+ \in \mathbf{H^1} : \mathbf{v}^+ = \mathbf{0} \qquad \mathbf{x} \in \Gamma_u^+\} \qquad \mathbf{u}^- \in \mathbf{U} = \{\mathbf{v}^- \in \mathbf{H^1} : \mathbf{v}^- = \mathbf{0} \qquad \mathbf{x} \in \Gamma_u^-\} \tag{7}$$

where H^1 is the space of functions with square-integrable derivatives (*i.e.*, the Sobolev space of degree 1). Equations (1)-(7) can be converted into a weak form using the principle of virtual work. Its application to the two subdomains Ω^+ and Ω^- leads to

$$\int_{\Omega^+} \boldsymbol{\sigma}^+(\mathbf{x}) : \boldsymbol{\epsilon}^+(\mathbf{v}^+(\mathbf{x}))d\Omega = \int_{\Gamma_t^+} \mathbf{t}^+_{\mathbf{ext}}(\mathbf{x}).\mathbf{v}^+(\mathbf{x})d\Gamma + \int_{\Gamma_c^+} \mathbf{t}^+_{\mathbf{int}}(\mathbf{x}).\mathbf{v}^+(\mathbf{x})d\Gamma \qquad \forall\mathbf{v} \in \mathbf{U} \tag{8}$$

$$\int_{\Omega^-} \boldsymbol{\sigma}^-(\mathbf{x}) : \boldsymbol{\epsilon}^-(\mathbf{v}^-(\mathbf{x}))d\Omega = \int_{\Gamma_t^-} \mathbf{t}^-_{\mathbf{ext}}(\mathbf{x}).\mathbf{v}^-(\mathbf{x})d\Gamma + \int_{\Gamma_c^-} \mathbf{t}^-_{\mathbf{int}}(\mathbf{x}).\mathbf{v}^-(\mathbf{x})d\Gamma \qquad \forall\mathbf{v} \in \mathbf{U} \tag{9}$$

The left-hand sides of equations (8) and (9) are the internal virtual work, the right-hand sides are the virtual work carried out by the external forces and the tractions along the strong discontinuity surface. The existence of a traction-free strong discontinuity surface translates into the following condition:

$$\mathbf{t}^-_{\mathbf{int}}(\mathbf{x}) = \mathbf{t}^+_{\mathbf{int}}(\mathbf{x}) = \mathbf{0} \quad \mathbf{x} \in \Gamma_c \tag{10}$$

The subdomains Ω^+ and Ω^- are now discretized with finite elements. Let $\{d^+\}$ and $\{d^-\}$ be the vectors of degrees of freedom of Ω^+ and Ω^- respectively. The displacement field in each sub-domain is obtained thanks to standard FE shape function matrices $[N^+]$ and $[N^-]$:

$$\mathbf{u}^+(\mathbf{x}) = [N^+(\mathbf{x})]\{d^+\} \qquad \mathbf{x} \in \Omega^+ \qquad\qquad \mathbf{u}^-(\mathbf{x}) = [N^-(\mathbf{x})]\{d^-\} \qquad \mathbf{x} \in \Omega^- \tag{11}$$

These shape functions are expressed as if the strong discontinuity surfaces were defined from the onset of the numerical calculation using a conforming mesh. Substitution of (11) into the weak forms (8) and (9) followed by the standard Bubnov–Galerkin approach leads to the discretized equilibrium equations

$$[L^+]\{d^+\} = \begin{Bmatrix} fext^+ \\ fcohesive^+ \end{Bmatrix} \qquad\qquad [L^-]\{d^-\} = \begin{Bmatrix} fext^- \\ fcohesive^- \end{Bmatrix} \tag{12}$$

where $[L^+]$ and $[L^-]$ are the stiffness matrices of the two subdomains, $\{fext^+\}$ and $\{fext^-\}$ are the external force vectors induced by the external tractions and $\{fcohesive^+\}$ and $\{fcohesive^-\}$ are the equivalent force vectors induced by the tractions on the strong discontinuity surface such that

$$[L^+] = \int_{\Omega^+} [B^+(\mathbf{x})]^t [\mathbf{C}^+][B^+(\mathbf{x})] d\Omega \qquad\qquad [L^-] = \int_{\Omega^-} [B^-(\mathbf{x})]^t [\mathbf{C}^-][B^-(\mathbf{x})] d\Omega \tag{13}$$

$$\{fext^+\} = \int_{\Gamma_t^+} [N^+(\mathbf{x})]\mathbf{t}^+_{\mathbf{ext}}(\mathbf{x}) d\Gamma \qquad\qquad \{fext^-\} = \int_{\Gamma_t^-} [N^-(\mathbf{x})]\mathbf{t}^-_{\mathbf{ext}} d\Gamma \tag{14}$$

$$\{fcohesive^+\} = \int_{\Gamma_c^+} [N^+(\mathbf{x})]\mathbf{t}^+_{\mathbf{int}}(\mathbf{x}) d\Gamma \qquad\qquad \{fcohesive^-\} = \int_{\Gamma_c^-} [N^-(\mathbf{x})]\mathbf{t}^-_{\mathbf{int}}(\mathbf{x}) d\Gamma \tag{15}$$

Equation (13) introduces the strain-displacement matrices, $[B^+]$ and $[B^-]$, which contain the derivatives of the classical FE shape functions (see, *e.g.*, [31] section 2.5). Substitution of (10) into (15) leads to:

$$\{fcohesive^+\} = \{fcohesive^-\} = \{0\} \tag{16}$$

The degrees of freedom vectors in (11) are further partitioned between those associated with the strong discontinuity surface (called $\{dint^+\}$ and $\{dint^-\}$) and those associated with the bulk (called $\{dext^+\}$ and $\{dext^-\}$).

$$\{d^+\} = \begin{Bmatrix} dext^+ \\ dint^+ \end{Bmatrix} \qquad\qquad \{d^-\} = \begin{Bmatrix} dext^- \\ dint^- \end{Bmatrix} \tag{17}$$

This partition is used to rewrite (12) the following way:

$$\begin{bmatrix} L_{11^+} & L_{12^+} \\ L_{21^+} & L_{22^+} \end{bmatrix} \begin{Bmatrix} dext^+ \\ dint^+ \end{Bmatrix} = \begin{Bmatrix} fext^+ \\ 0 \end{Bmatrix} \qquad\qquad \begin{bmatrix} L_{11^-} & L_{12^-} \\ L_{21^-} & L_{22^-} \end{bmatrix} \begin{Bmatrix} dext^- \\ dint^- \end{Bmatrix} = \begin{Bmatrix} fext^- \\ 0 \end{Bmatrix} \tag{18}$$

Relations (18) allow to express the displacement at the discontinuity as a function of the external displacement:

$$\{dint^+\} = -[L_{22^+}]^{-1}[L_{21^+}]\{dext^+\} \qquad\qquad \{dint^-\} = -[L_{22^-}]^{-1}[L_{21^-}]\{dext^-\} \tag{19}$$

Substitution of (19) into (18) allows to eliminate $\{dint^+\}$ and $\{dint^-\}$ from the discretized equilibrium equations. The resulting relation is called the condensed discretized equilibrium equation and reads

$$\{fext\} = \begin{bmatrix} L_{11}^- - L_{12^-}L_{22^-}^{-1}L_{21^-} & 0 \\ 0 & L_{11}^+ - L_{12^+}L_{22^+}^{-1}L_{21^+} \end{bmatrix} \{dext\} \tag{20}$$

where

$$\{dext\} = \begin{Bmatrix} dext^- \\ dext^+ \end{Bmatrix} \qquad \{fext\} = \begin{Bmatrix} fext^- \\ fext^+ \end{Bmatrix} \tag{21}$$

Equation (20) introduces the stiffness matrix of the augmented finite elements. These element matrices are assembled to form the global matrix of the system. Since $\{dint^+\}$ and $\{dint^-\}$ do not appear in the condensed discretized equilibrium equation (20), the nodes associated with these DOF, called internal nodes (see Figure 3) do not contribute to the size of the global stiffness matrix. As highlighted by Equation (11), the AFEM and the classical FEM make use of the same shape functions to describe the displacement field on both sides of a strong discontinuity. The main difference between the FEM and the AFEM lies in the fact that the internal nodes (see Figure 3) are condensed at the element level with the AFEM. As a result, the DOF associated with these internal nodes are absent from the discretized equilibrium equation (20). Hence, the AFEM can model an arbitrary number of strong discontinuities without modifying the number of DOF per element or the size of the assembled stiffness matrix. This attractive property, not shared by the FEM or the XFEM, comes at a price: since the internal nodes are condensed at the element level, the interelement compatibility is lost.

Equation (20) has been derived under the assumption of a traction-free crack. It thus differ from the condensed discretized equilibrium of the original AFEM which contains additional terms linked to the existence of cohesive stresses, see, *e.g.*, Equation 19 in [19]. One can nevertheless check that the former equation reduces to (20) when cohesive stresses are null. Hence, as stated in the introduction of the present section, the AFEM we just derived and the original AFEM are fully equivalent in the presence of traction-free cracks.

The compactness of the traction-free crack discretized equilibrium, (20), greatly facilitates comparisons of the AFEM with other newly developed EFEMs. For instance, one can readily check that the AFEM, the so-called continuum decohesive finite element method [49] and the extended cohesive damage model [50] share the very same discretized condensed equilibrium equation (see, *e.g.*, equation 12 in [50]). The only difference between the AFEM and the two aforementioned methods lies in the technique employed to account for the cohesive stresses. Thus, the use of any of these methods will deliver identical results if traction-free cracks are modelled, which is the topic of this paper.

The compactness of the traction-free discretized equilibrium equation (20) also highlights some flaws of the AFEM (which equally affect the continuum decohesive finite element method and the extended cohesive damage model). Indeed, the use of the former equation requires the invertibility of some stiffness submatrices. These submatrices invertibility is related to *i)* the parent element employed (*i.e.*, constant strain triangular element, bilinear quadrilateral element, etc.) and to *ii)* the location of the crack within the element. As will be shown later, the use of constant strain triangular elements unavoidably induces the singularity of the aforesaid submatrices. To the authors best knowledge, this topic of prime importance has only been briefly discussed in [18] without being satisfactorily resolved. The next chapter particularizes the above equations to 2D elements while dealing with this issue.

3.2. Application to the 2D elements of this study

The condensed discretized equilibrium equation (20) can be applied to parent elements of any dimension and order. Particularization to 2D elements with linear shape functions is considered next. The parent elements used in this study are the constant strain triangle, called hereafter T3, and the bilinear quadrilateral called Q4. A strong

discontinuity splits a T3 into a triangular domain and a quadrangle, the resulting element is called an AT3. When a Q4 is augmented, two situations can occur depending on the location of the discontinuity *i)* it is split into two quadrangles and the resulting element is named AQ4-1 or *ii)* it is split into a triangle and a pentagon, the resulting element is called AQ4-2, see Figure 3. As stated in the introduction, the most salient feature of the AFEM is that augmented elements and their parent elements share the same degrees of freedom, see Table 1. In this study, the

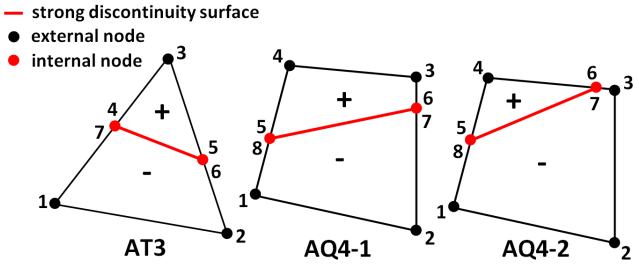

Figure 3: Node numbering of the augmented elements used in this study

stiffness matrices of quadrilateral and triangular subdomains are computed thanks to a 2×2 points Gauss integration scheme and a 1-point integration scheme respectively. Pentagonal elements, called P5, are implemented using the polygonal finite element method proposed by Sukumar and co-workers [51]. A 6-point integration scheme has been used to evaluate the stiffness matrices of the P5 used in this study.

Table 1: Degrees of freedom of the augmented elements used in this study

Augmented Element	$\{dext^+\}^t$	$\{dext^-\}^t$	$\{dint^+\}^t$ (condensed DOF)	$\{dint^-\}^t$ (condensed DOF)
AT3	$\{u_3, v_3\}$	$\{u_1, v_1, u_2, v_2\}$	$\{u_4, v_4, u_5, v_5\}$	$\{u_7, v_7, u_6, v_6\}$
AQ4-1	$\{u_3, v_3, u_4, v_4\}$	$\{u_1, v_1, u_2, v_2\}$	$\{u_5, v_5, u_6, v_6\}$	$\{u_8, v_8, u_7, v_7\}$
AQ4-2	$\{u_4, v_4\}$	$\{u_1, v_1, u_2, v_2, u_3, v_3\}$	$\{u_5, v_5, u_6, v_6\}$	$\{u_8, v_8, u_7, v_7\}$

The condensed discretized equilibrium equation (20) makes use of the inverse of matrices $\left[L_{22}^+\right]$ and $\left[L_{22}^-\right]$. As highlighted by Equation (18), $[L_{22}^\pm]$ are submatrices of $[L^\pm]$. A mechanical interpretation of the involved submatrices is now provided to ease the study of their invertibility. Submatrices $[L_{22}^\pm]$ appear when one incorporates essential boundary conditions in the stiffness matrix by the method of reduction (see, *e.g.*,[52]). To illustrate this fact, suppose that one seeks to impose the essential boundary conditions $\{dext^\pm\} = \{0\}$ in equation (12) thanks to the method of reduction. The discretized equilibrium equations in Ω^+ and Ω^- would write:

$$\begin{bmatrix} L_{11^\pm} & L_{12^\pm} \\ L_{21^\pm} & L_{22^\pm} \end{bmatrix} \begin{Bmatrix} dext^\pm \\ dint^\pm \end{Bmatrix} = \begin{bmatrix} L_{11^\pm} & L_{12^\pm} \\ L_{21^\pm} & L_{22^\pm} \end{bmatrix} \begin{Bmatrix} 0 \\ dint^\pm \end{Bmatrix} = \begin{Bmatrix} fext^\pm \\ fcohesive^\pm \end{Bmatrix} \tag{22}$$

To solve for the unconstrained degrees of freedom, $\{dint^\pm\}$, one needs to invert the stiffness submatrices $[L_{22^\pm}]$:

$$\left\{dint^\pm\right\} = \left[L_{22^\pm}\right]^{-1} \left\{fcohesive^\pm\right\} \tag{23}$$

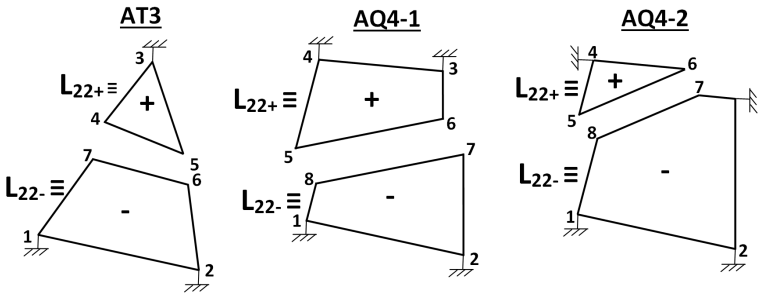

Figure 4: Graphical representation of the submatrices $[L_{22^{\pm}}]$ of 2D elements

Thus, $[L_{22^+}]$ (respectively $[L_{22^-}]$) is the stiffness matrix of the subdomain Ω^+ (respectively Ω^-) with degrees of freedom $\{dext^+\}$ (respectively $\{dext^-\}$) fully constrained. A graphical representation of these submatrices is proposed for the 2D augmented elements of this study in Figure 4. This graphical representation allows to readily assess the ranks of submatrices $\left[L_{22^{\pm}}\right]$. If rigid body motions of the subdomains are allowed, the associated submatrices are singular (see, *e.g.*, [31] chapter 2.8 for a proof). Hence, submatrices $[L_{22^+}]$ of elements AQ4-2 and AT3, are singular since the rotation of the associated subdomains is not prevented, see Figure 4. As a result, the condensed discretized equilibrium equation (20) is not applicable to these elements. To circumvent these singularities, the authors of the AFEM suggested to not fully relax the cohesive stresses, which stabilizes the elements [19]. Nevertheless, this approach prevents the modelling of truly traction-free cracks. Moreover, the amount of cohesive stresses needed to stabilize the elements is not discussed. Singular stiffness submatrices also arise in other EFEM formulations, see, *e.g.* [44–46]. To suppress these singularities some authors impose kinematic constraints on the crack opening: a constant opening is often enforced. This may induce stress-locking [44, 45] or involve the use of a problem-dependent stabilization parameter that needs to be calibrated [45, 46]. In this paper we propose a parameter-free way to deal with the inversion of singular matrices: we compute the Moore-Penrose inverse (also called pseudo-inverse) of the singular matrices. Some useful properties of pseudo-inverses are briefly recalled *i)* the pseudo-inverse of a matrix always exists and is unique, *ii)* if a matrix $[M]$ is invertible, its pseudo-inverse equals its inverse: $M^{-1} = M^{\dagger}$. As a result, the use of the pseudo-inverses does not affect the formulation of the AQ4-1 whose submatrices, $[L_{22^+}]$, are invertible. A great advantage of this "pseudo-inverse strategy" is that the modification with respect to the original derivation is minimal: equation (19) is rewritten

$$\{dint^+\} = -[L_{22^+}]^{\dagger}[L_{21^+}]\{dext^+\} \qquad \{dint^-\} = -[L_{22^-}]^{\dagger}[L_{21^-}]\{dext^-\} \tag{24}$$

and equation (20) becomes

$$\{fext\} = \begin{bmatrix} L_{11}^- - L_{12^-}L_{22^-}^{\dagger}L_{21^-} & 0 \\ 0 & L_{11}^+ - L_{12^+}L_{22^+}^{\dagger}L_{21^+} \end{bmatrix} \{dext\} \tag{25}$$

4. NUMERICAL BENCHMARKS

This section presents the results obtained in a series of numerical tests designed to evaluate the performance of the augmented finite element method (AFEM). The absence of stress locking in augmented finite elements is confirmed thanks to the partial tension test performed in Section 4.1. Section 4.2 focuses on the stiffness loss induced by the presence of a crack in a structure, and compares the performances of the AFEM, the element deletion method (EDM),

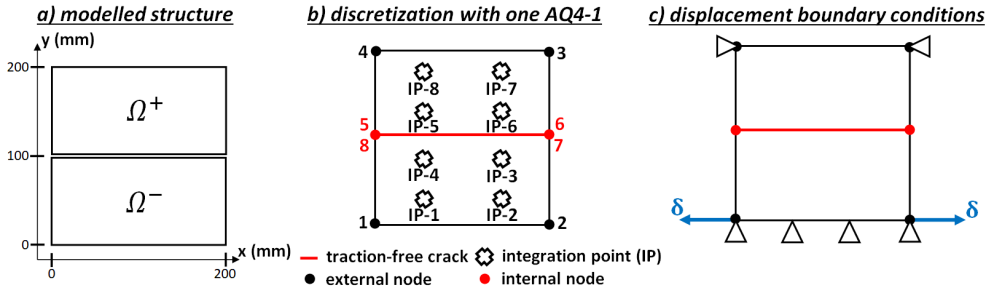

Figure 5: Element partial tension test: a) geometry definition, b) employed discretization, c) boundary conditions

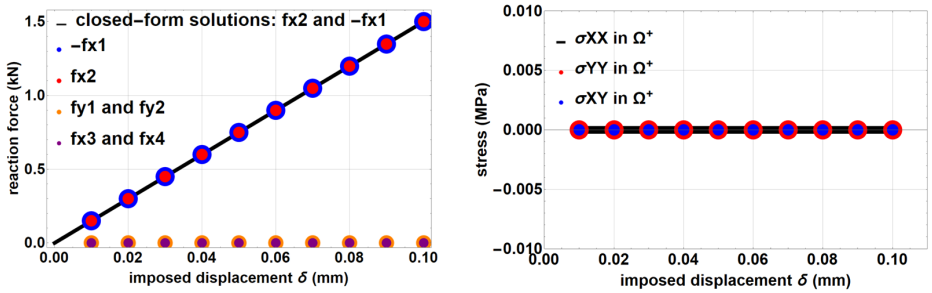

Figure 6: Reaction forces and stresses in the subdomain Ω^+ measured through the partial tension test

the finite element method (FEM) and the phantom node method (PNM). The convergence rate in the energy norm of the AFEM, the FEM and the EDM is studied in Section 4.3, under Mode I and Mode II loading conditions. Finally, the accuracy at which stress intensity factors can be computed with these methods is evaluated in Section 4.4.

4.1. Partial tension test

The partial tension test is a numerical experiment designed by Linder and Armero to assess the level of stress locking of some embedded finite element methods (EFEMs) [45]. Slightly modified versions of this test can also be encountered in the literature [3, 46]. Linder and Armero showed that classical EFEMs, *i.e.*, with a constant crack opening, failed this test and that the use of embedded finite element methods with enhanced strain modes (EFEM-SM) was compulsory to pass it [45]. The partial tension test consists in modelling a homogeneous square block, cut in half by a traction-free crack, see Figure 5 a. The block is discretized with a single augmented element: the AQ4-1 presented in Section 3.2, see Figure 5 b. We recall that, although the AQ4-1 embeds a crack, its stiffness matrix is only 8×8; the choice of the PNM or the FEM to model the cracked block would result in the use of a 16×16 stiffness matrix. Horizontal displacements of equal magnitudes δ, but opposite directions, are imposed on the bottom corner nodes of the cracked structure, leading to an axial stretching of the lower subdomain, denoted as Ω^-, see Figure 5 c. The test is passed if the upper domain, Ω^+, is stress-free and if no reaction forces are measured on the nodes located in Ω^+. We made use of the same geometry, material properties and load steps as in [45]: a plane stress state is assumed, the block side length is $L = 200mm$, the Young's modulus is $E = 30GPa$, the Poisson's ratio is $\nu = 0$, the total displacement is $\delta = 0.1mm$ and it is applied in 10 steps. The reaction forces and the stresses at the four integration points located in Ω^+ are plotted in Figure 6. It can be seen that the test is passed: the subdomain Ω^+ is stress-free and the

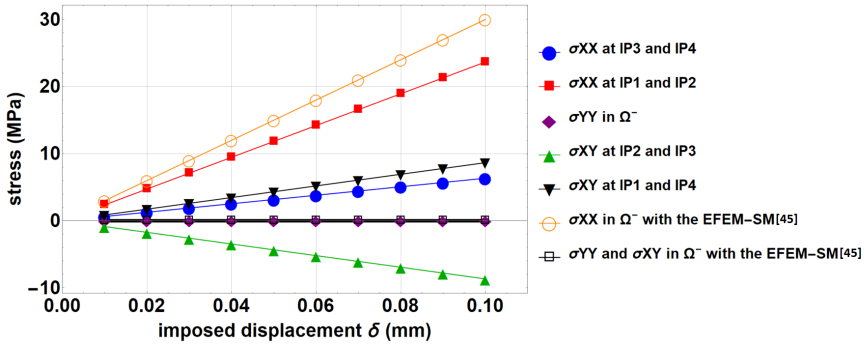

Figure 7: Comparisons of stresses in Ω^- at given integration points (IP), obtained with the AFEM and the EFEM-SM[45] through the partial tension test

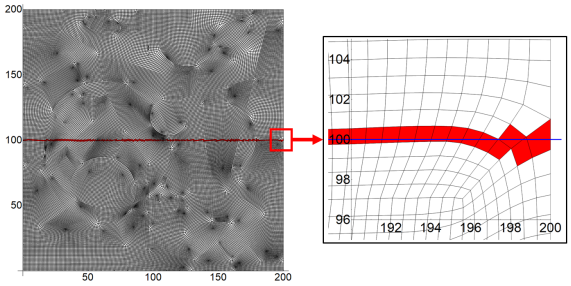

Figure 8: Refined mesh, made of randomly oriented elements, used to run the element partial tension test, augmented elements are represented in red and standard bilinear finite elements are coloured in white

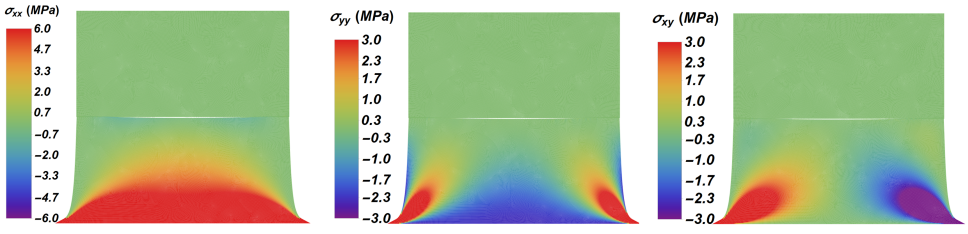

Figure 9: Partial tension test: stress state obtained with the refined mesh and an imposed displacement $\delta = 0.1mm$, displacements are magnified 200 times

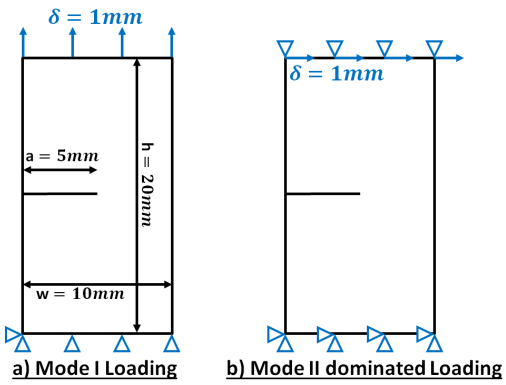

Figure 10: Geometry and boundary conditions of the cracked plate submitted to a) Mode I loading, b) Mode II dominated loading

reaction forces at nodes 3 and 4 are null. It is demonstrated that the reaction forces exerted on the augmented element are consistent with those predicted by the FEM: indeed, if Ω^- was modelled with a standard bilinear quadrilateral element (Q4), one would have $-f_{x1}(\delta) = f_{x2}(\delta) = \frac{\delta E(\nu(3\nu+2)-6)}{12(\nu^2-1)}$ (the proof is provided in Appendix A). It is also instructive to inspect the stresses measured in the lower subdomain, Ω^-, and to compare them with those obtained with the EFEM-SM of Linder and Armero[45]. As highlighted by Figure 7, the EFEM-SM predicts a constant uniaxial stress state in Ω^- while a multiaxial and heterogeneous stress state is obtained with the AFEM. To get a better insight into the exact stress state in Ω^-, we discretized the cracked block with a refined mesh comprising around 50000 quadrilateral elements and 100000 degrees of freedom, see Figure 8. The crack is once again modelled with augmented finite elements (AQ4-1 and AQ4-2) while the other elements are classical Q4. The boundary conditions represented in Figure 5 c are imposed with $\delta = 0.1mm$. The resulting stress field is plotted in Figure 9. It is heterogeneous and multiaxial, as predicted with a single augmented element. Cross-checking the results presented in Figure 9 and Figure 7 allows to thoroughly evaluate the predictions made with a single AQ4-1. The stress sate obtained with the refined mesh is σ_{xx}-dominated, σ_{xx} decreases as y increases, σ_{yy} is approximately null at the location of the integration points 1 to 4 represented in Figure 5 b and σ_{xy} is positive (respectively negative) in the bottom right (respectively left) corner. All these results were decently assessed with a single augmented element, as depicted in Figure 7.

4.2. Crack-induced stiffness loss

To further compare the AFEM and the EFEM-SM, we perform a numerical experiment, designed by Linder and Armero, that consists in measuring the stiffness of a cracked plate as the mesh is refined [45]. To enrich the comparison, we also benchmark the element deletion method (EDM), the finite element method (FEM) and the phantom node method (PNM). The geometry of interest is a cracked rectangular plate, with a height $h = 20mm$, a width $w = 10mm$ and a crack length $a = 5mm$, see Figure 10. As in[45], plane strain conditions are assumed, the Young's modulus is $E = 206.9GPa$, the Poisson's ratio is $\nu = 0.29$ and we only consider structured meshes made of quadrilateral elements. A vertical displacement, $\delta = 1mm$, is imposed on the upper edge of the plate and induces a Mode I loading of the crack, see Figure 10 a. The evolution of the associated reaction force is plotted in Figure 11. One can observe that all the benchmarked methods seem to converge toward the same reaction force as the mesh is refined. The EDM, the AFEM and the EFEM-SM produce virtually identical results and give rise to models that are softer than the actual

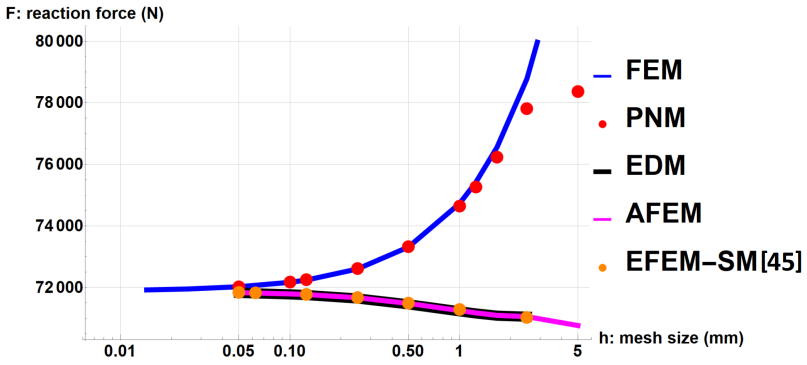

Figure 11: Mode I loading: reaction force as a function of the mesh size obtained with the FEM, the PNM, the EDM, the AFEM and the EFEM-SM of Linder and Armero[45]

structure as they systematically underestimate the reaction forces. This was also observed when using the AFEM to model weak discontinuities, and was proved to be caused by the presence of interelement discontinuities[53]. It strongly contrasts with the standard FEM and the PNM that are known to overestimate the stiffness[31–33].

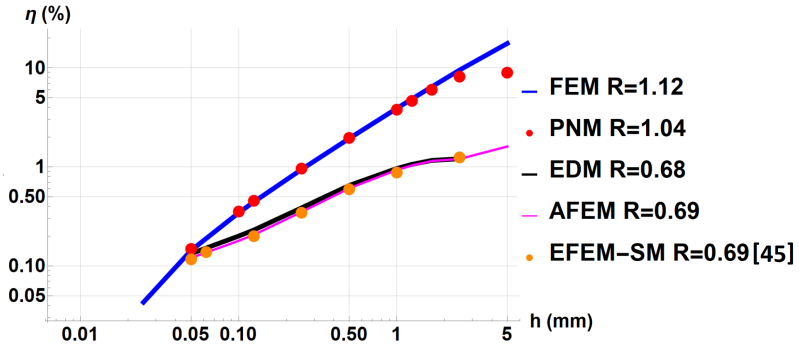

Figure 12: Mode I loading: relative error in reaction force, η, as a function of the mesh size, h, and associated asymptotic convergence rate, R, obtained with the FEM, the PNM, the EDM, the AFEM and the EFEM-SM[45]

To get a better insight into the error levels of the benchmarked methods, we have computed the relative error in reaction force, defined as:

$$\eta = 100\% \times \frac{|\widehat{f_{reaction}} - f_{reaction}|}{f_{reaction}} \tag{26}$$

where $f_{reaction}$ is the exact reaction force and $\widehat{f_{reaction}}$ is the reaction force computed with the numerical methods. In this study, the "exact" reaction force is estimated with the finest FEM mesh of Figure 11 which comprises around 1 million elements. The relative error in reaction force, along with the associated convergence rates, is plotted in Figure 12. It clearly highlights the different asymptotic convergence rates of the benchmarked methods: the EDM, the AFEM and the EFEM-SM converge with an error of $\mathcal{O}(h^{0.7})$ while the FEM and the PNM converge at approximately $\mathcal{O}(h)$. Despite their faster convergence rate, the latter methods perform worse than the EDM, the AFEM and the EFEM-SM for element sizes ranging from $5mm$ to $50\mu m$. Hence, unless a "highly refined" mesh is employed, a method as crude as the EDM outperforms advanced modelling techniques such as the PNM (in the authors' opinion, a mesh made of

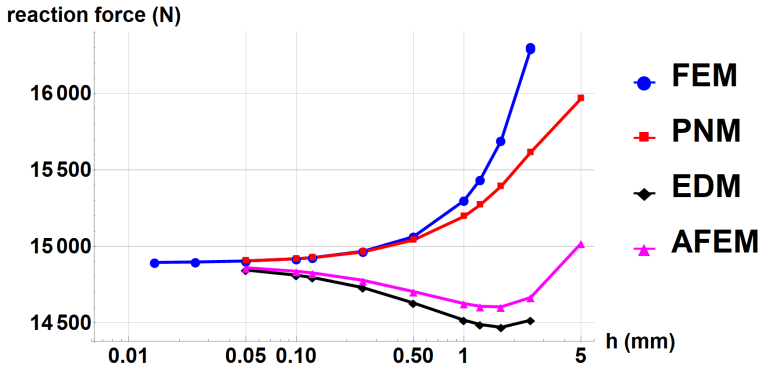

Figure 13: Mode II loading: reaction force as a function of the mesh size provided by the FEM, the PNM, the EDM and the AFEM

$50\mu m$ elements can already be considered as "highly refined" since the structure is $10mm$ wide). The EFEM-SM and the AFEM perform slightly better than the EDM but the differences are marginal, see Figure 12.

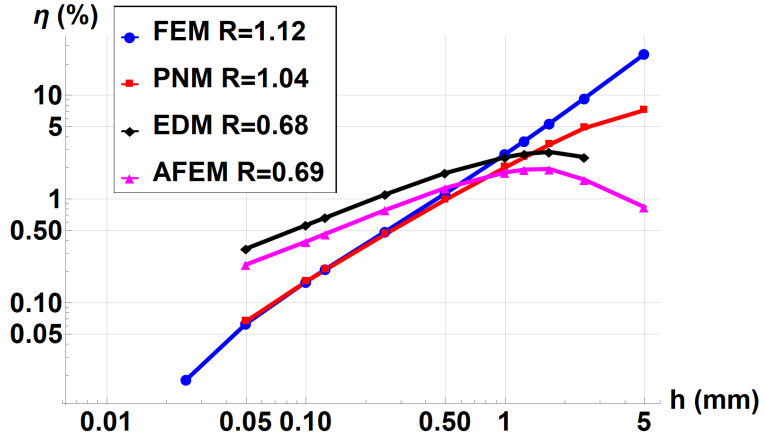

Figure 14: Mode II loading: relative error in reaction force, η, as a function of the mesh size, h, and associated asymptotic convergence rate, R, obtained with the FEM, the PNM, the EDM and the AFEM

It is instructive to evaluate the performances of the studied numerical methods under a loading of the crack that is Mode II dominated. To generate such a loading, we made use of the boundary conditions depicted in Figure 10 b where a horizontal displacement, $\delta = 1mm$, is imposed on the upper edge of the plate. The evolution of the associated reaction force is plotted in Figure 13. The EFEM-SM is no longer part of the comparisons since no result could be found in the literature with these boundary conditions. As observed in Mode I, all the methods seem to converge toward the same value, the FEM and the PNM are stiffer than the actual structure and the EDM and the AFEM are systematically softer than the solid they are modelling. The PNM and the FEM provide notably different results with the coarsest meshes, which is surprising and contrasts with other observations[39]. As mentioned in Section 2.3, we made use of the PNM implemented in Abaqus v6.16 and no indications regarding the integration scheme of the associated elements have been found in the documentation. It is likely that the PNM implemented in Abaqus make use of selective reduced integration schemes, which often outperforms full integration schemes as the one we

employed with the Q4, (see, *e.g.*, Chapter 9.9[32]). The asymptotic convergence rates are nevertheless not affected by this feature. To get a better insight into the error levels of the benchmarked methods, the evolution of the relative error in reaction force with mesh refinement is plotted in Figure 14. It can be seen the asymptotic convergence rates of the numerical methods are the same as in Mode I. For the coarsest meshes the EDM and the AFEM exhibit a non-monotonic behaviour as the error may increase as the mesh is refined. Nevertheless, in the present test case, the range of mesh sizes where this non-monotonic behaviour is observed coincides with the region where the AFEM outperforms both the FEM and the PNM (*i.e*, for mesh size ranging from $5mm$ to $0.9mm$). Hence, despite the fact that the convergence rate of the AFEM is not monotonic in Mode II, the AFEM is more "coarse mesh accurate" than the FEM or the PNM. One also notices that the AFEM performs better than the EDM in Mode II: it is approximately twice as accurate as the EDM for a given element size.

4.3. h-convergence in the energy norm

In this section we will focus on the error in the energy norm, rather than on the computation of some local quantities (*e.g.*, the reaction forces). This error measure is at the core of some fundamental properties of the FEM, such as the Galerkin orthogonality (see, *e.g.*, Chapter 4.3 [33] and references therein), and is frequently employed to assess the convergence behaviour of the FEM and its variants. Since the use of the AFEM induces interelement discontinuities, its monotonic convergence toward the exact solution of a mathematical problem cannot be guaranteed (see, *e.g.*, Chapter 4.4 [33]). The goal of this section is to study the AFEM convergence behaviour, in the energy norm, through numerical experiments. Comparisons with the finite element method (FEM) and the element deletion method (EDM) will also be drawn and the performances of both triangular and quadrilateral elements will be investigated. Let us first introduce the error in the energy norm, as well as some related quantities, before presenting the tests performed in this section. Let $\mathbf{u}$ be the exact solution of a mechanical problem and $\hat{\mathbf{u}}$ an approximate solution, the error $\mathbf{e}$ is defined by:

$$\mathbf{e} = \mathbf{u} - \hat{\mathbf{u}} \tag{27}$$

Let Ω be the volume occupied by the structure of interest, the error in the energy norm reads:

$$||\mathbf{e}||_\Omega = \left(\int_\Omega (\epsilon - \hat{\epsilon}) : C : (\epsilon - \hat{\epsilon}) \, d\Omega \right)^{\frac{1}{2}} \tag{28}$$

where ϵ is the exact strain field, $\hat{\epsilon}$ the approximate one and C the elasticity tensor. We will also make use of the energy error of a given finite element, defined as:

$$||\mathbf{e}||_{\Omega_i} = \left(\int_{\Omega_i} (\epsilon - \hat{\epsilon}) : C : (\epsilon - \hat{\epsilon}) \, d\Omega \right)^{\frac{1}{2}} \tag{29}$$

where the subscript i refers to individual elements such that $\bigcup_i \Omega_i = \Omega$. We finally introduce the relative error in the energy error norm, $||\eta||$:

$$||\eta|| = \left(\frac{\int_\Omega (\epsilon - \hat{\epsilon}) : C : (\epsilon - \hat{\epsilon}) \, d\Omega}{\int_\Omega \epsilon : C : \epsilon \, d\Omega} \right)^{\frac{1}{2}} \tag{30}$$

To investigate the AFEM convergence, we perform a test case often encountered in the XFEM literature [16, 17]: an infinite plate containing a horizontal crack is loaded by a remote stress field. We successively consider Mode I and Mode II loading of the crack. Plane strain is assumed and the material is homogeneous and isotropic with a Young's

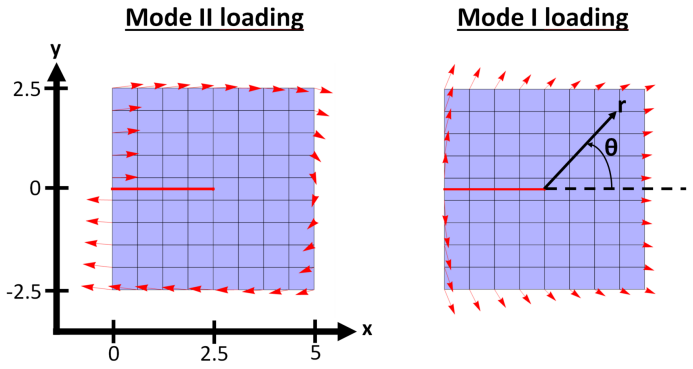

Figure 15: Geometry, polar coordinate system and displacement boundary conditions imposed on the boundary of the plate in Mode I and Mode II loadings

modulus E and a Poisson's ratio ν. The analytical solution of the asymptotic displacement field under Mode I loading, denoted as $u_I = \{u_I x, u_I y\}$, reads[54]:

$$u_I x = \frac{K_I}{E}\sqrt{\frac{r}{2\pi}}(1+\nu)cos\left(\frac{\theta}{2}\right)(3-4\nu-cos(\theta)) \tag{31}$$

$$u_I y = \frac{K_I}{E}\sqrt{\frac{r}{2\pi}}(1+\nu)sin\left(\frac{\theta}{2}\right)(3-4\nu-cos(\theta)) \tag{32}$$

where K_I is the Mode I stress intensity factor and (r, θ) are the polar coordinates associated with a reference frame centered at the crack tip, as depicted in Figure 15. The closed-form solution of the displacement field under Mode II loading, denoted as u_{II}, is[54]:

$$u_{II} x = \frac{K_{II}}{E}\sqrt{\frac{r}{2\pi}}(1+\nu)sin\left(\frac{\theta}{2}\right)(5-4\nu+cos(\theta)) \tag{33}$$

$$u_{II} y = \frac{K_{II}}{E}\sqrt{\frac{r}{2\pi}}(1+\nu)cos\left(\frac{\theta}{2}\right)(-1+4\nu-cos(\theta)) \tag{34}$$

In the numerical model we consider a square domain $\Omega = [0,5] \times [-2.5, 2.5]$ cut by a crack $\Gamma_c = [0, 2.5] \times \{0\}$. Young's modulus and Poisson's ratio are respectively $E = 200000$ and $\nu = 0.3$, and the imposed stress intensity factors are $K_I = K_{II} = 2802,5$. Following Laborde and co-workers[17], we impose the closed-form displacement field on the boundary of the plate, as depicted in Figure 15. The evolution of the error in the energy norm with the mesh size, under Mode I loading of the crack, is plotted in Figure 16. It is shown that the FEM, the EDM and the AFEM are of similar accuracy. When quadrilateral elements are considered, the AFEM slightly outperforms the aforesaid numerical methods, but the differences are marginal. The convergence rate of both the FEM, the AFEM and the EDM is subobtimal: $\mathcal{O}(h^{0.5})$ in the energy norm. The FEM suboptimal convergence is due to the crack-induced singularity of the stress field, as demonstrated by Pian and co-workers[36]. This reasoning seems to hold with the EDM and the AFEM, indeed, the spatial distribution of error is fairly independent of the employed numerical method under Mode I loading, see Figure 18 MODE I.

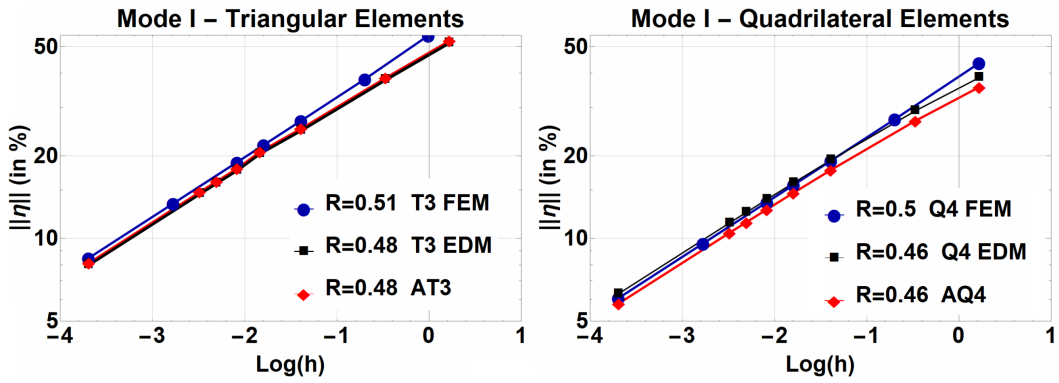

Figure 16: Mode I loading of a crack: error in the energy norm, $||\eta||$, as a function of the mesh size, h, and associated convergence rate, R, obtained with the finite element method (FEM), the element deletion method (EDM) and the augmented finite element method (AFEM)

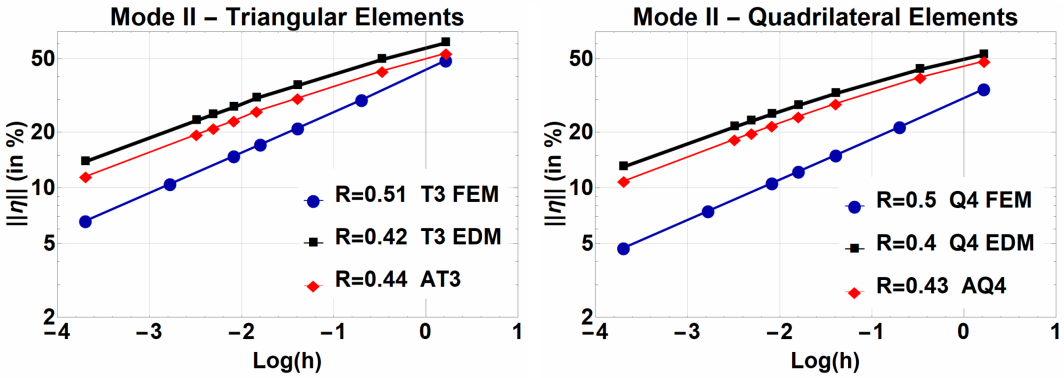

Figure 17: Mode II loading of a crack: error in the energy norm, $||\eta||$, as a function of the mesh size, h, and associated convergence rate, R, obtained with the (FEM), the element deletion method (EDM) and the augmented finite element method (AFEM)

The benchmarked numerical methods provide noticeably different results when Mode II loading of the crack is considered. Indeed, as depicted in Figure 17, the FEM is more accurate and converge faster than the AFEM and the EDM. Despite their similar converge rate, the AFEM is shown to be 25% more accurate than the EDM under Mode II loading. To gain further insights into these results, the spatial distribution of error is plotted in Figure 18. Conversely to the Mode I case, the energy error is no longer negligible along the crack lips when the EDM and the AFEM are employed.

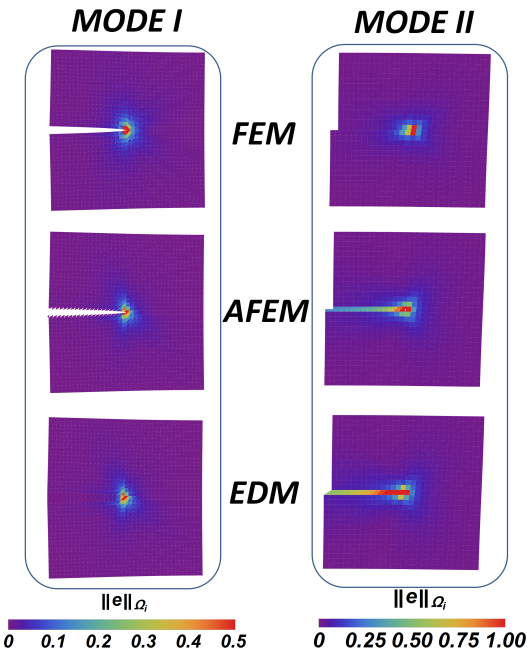

Figure 18: Spatial distribution of energy error in the elements, $||\mathbf{e}||_{\Omega_i}$, under Mode I and Mode II loadings, with the FEM, the AFEM and the EDM (results obtained with a mesh size $h \approx 0.15$)

The inter-element incompability of the displacement field, induced by the use of the AFEM, is thought to be responsible for its underperformance under Mode II loading of the crack. A so far unmentioned treatment helps reducing the amount of inter-element incompabilities: in Reference [19] Yang and colleagues implemented a simple "crack-tip treatment" that guarantees the inter-element continuity of the displacement field along the edge that is shared by the crack-tip element and the element immediately ahead of it, which is a standard finite element. The displacement continuity at the crack-tip is enforced through simple multiple-point constraints involving the nodal displacements at the considered edge, as illustrated in Figure 19. With the notations introduced in the aforesaid Figure, the multiple-point constraints to enforce read:

$$\left\{\begin{array}{c} u_6 \\ v_6 \end{array}\right\} = \left\{\begin{array}{c} u_7 \\ v_7 \end{array}\right\} = \left(1 - \frac{l_{72}}{l_{23}}\right) \left\{\begin{array}{c} u_2 \\ v_2 \end{array}\right\} + \frac{l_{72}}{l_{23}} \left\{\begin{array}{c} u_3 \\ v_3 \end{array}\right\} \tag{35}$$

where l_{72} and l_{23} are the lengths of segments 7-2 and 2-3, respectively.

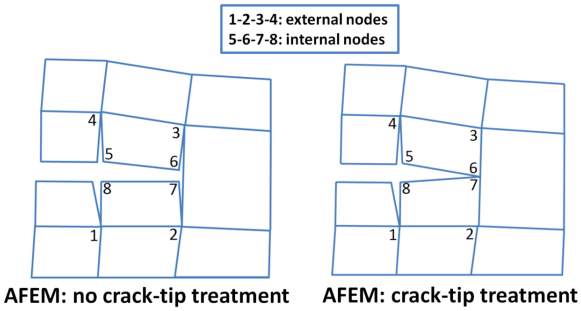

Figure 19: Crack-tip treatment allowing for a continuous displacement field along the edge shared by an augmented and a standard finite element

These multiple-point constraints are imposed thanks to Lagrange Multipliers introduced in Equation 18. The condensation procedure of the AFEM internal DOF, described in Section3.1, remains unchanged since no additional DOF have to be introduced at the global level. In the remainder of this work, the suffix "-TIP" will be employed to indicate simulations performed with the crack-tip treatment. As depicted in Figure 20, the use of the crack-tip treatment only slightly improves the results provided by the AFEM in Mode II. Hence, wether one uses the crack-tip treatment or not, the AFEM energy error is higher than the FEM one when cracks are loaded in pure Mode II.

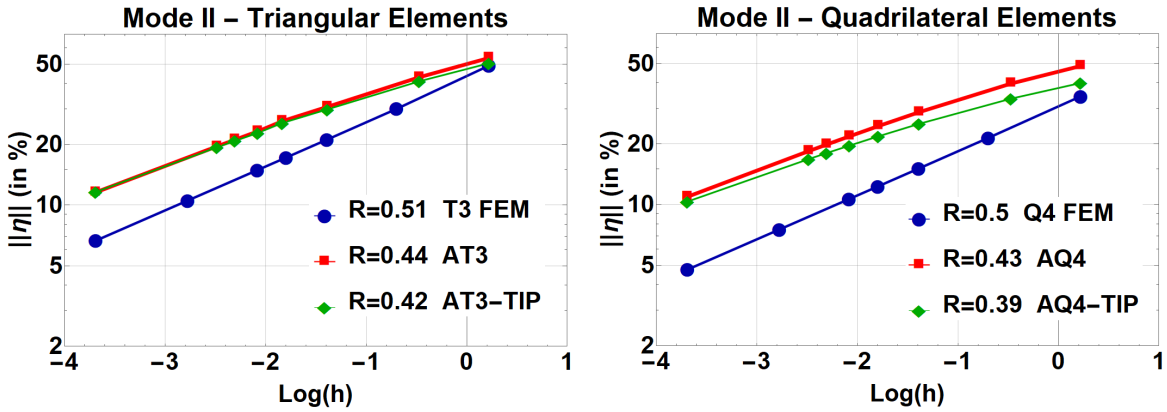

Figure 20: Influence of the crack-tip treatment, indicated by the suffix "-TIP", under Mode II loading of a crack: error in the energy norm, $||\eta||$, as a function of the mesh size, h, and associated convergence rate, R, with the FEM, the AFEM and the AFEM with a crack-tip treatment

To understand the reasons for this Mode II underperformance, we further studied the stress field in several zones of interest defined in Figure 21. As depicted in Figure 18, under Mode II loading of the crack, the most stricking difference between the AFEM and the standard FEM is the error level along the crack lips. The stress field provided by the AFEM in this area is compared with the exact stress field in Figure 22.

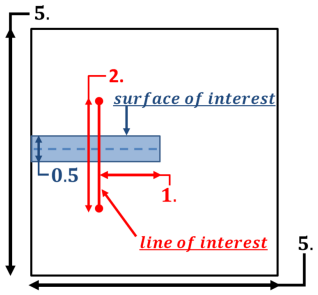

Figure 21: Zones of interest defined to study the stress field provided by the AFEM under Mode II loading of the crack

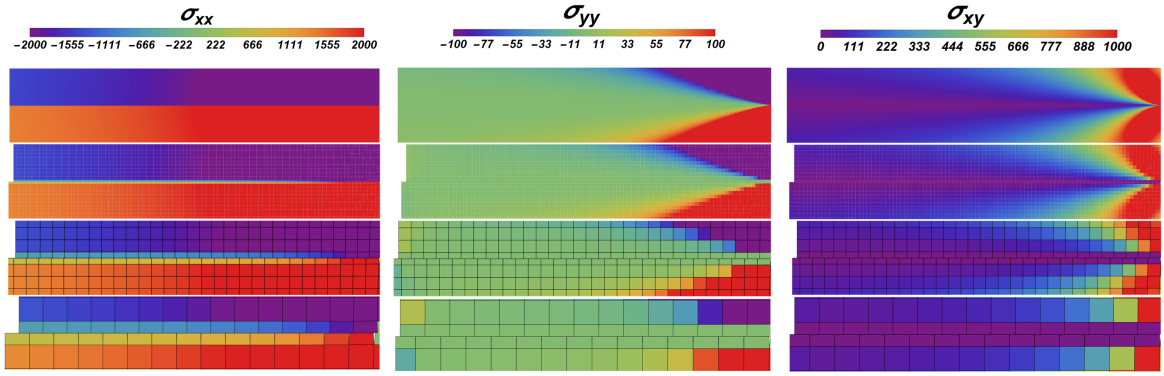

Figure 22: Comparisons of the exact stress field (on top) with those obtained with AQ4 elements and mesh sizes $h = 0.025, 0.15, 0.3$ (from top to bottom), within the surface of interest defined in Figure 21 and under Mode II loading of the crack

Whatever the mesh size, the stress field obtained with the AFEM is free from parasitic stresses and reproduces well the main characteristics of the exact stress field. A closer look at the transverse stress field, *i.e.* σ_{xx}, reveals that the stresses are too low within the augmented elements. Thus, the error in transverse stresses is responsible for the energy error observed all along the crack lips in Mode II (see Figure 18). To get quantitative insights on this aspect, the transverse stress along the line of interest defined in Figure 22 is plotted in Figure 23.

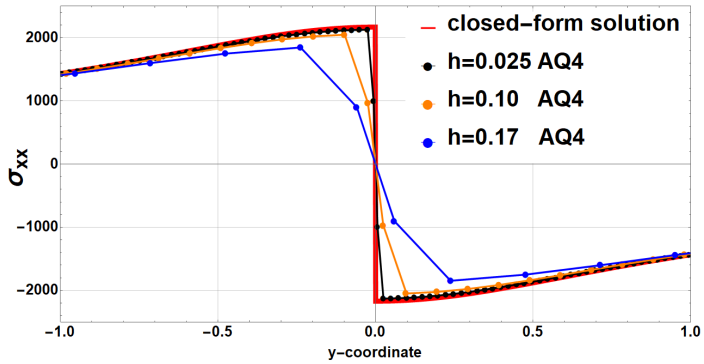

Figure 23: Comparisons of the exact transverse stress field, σ_{xx}, with those obtained with AQ4 elements, along the line of interest defined in Figure 21 and under Mode II loading of the crack

One can observe that σ_{xx} is approximately two times lower than expected in the immediate vicitiny of the crack lips. The convergence of this local value is noticeably slow. Despite this undesirable local attribute, the transverse stress is smooth and converges monotonically. These observations led us to the following conclusion: the inter-element discontinuities induce a local loss of transverse stiffness which has a detrimental effect on the energy error when crack lips are submitted to transverse loads. Hence, the use of the AFEM induces higher energy error levels than the standard FEM or the PNM when cracks are loaded in pure Mode II. While Figures 23 and 22 only highlight the results obtained with the AQ4 formulation, the above conclusions were found to be equally valid with the other augmented elements benchmarked in this study (*i.e.*, the $AT3$, the $AT3\text{-}TIP$ and the $AQ4\text{-}TIP$).

4.4. Computation of stress intensity factors (SIFs)

This final benchmark investigates the relative accuracy of the stress intensity factors (SIFs) computed with the finite element method (FEM), the element deletion method (EDM) and the augmented finite element method (AFEM). Accurate computations of SIFs is of prime importance in most of the crack growth analysis[34, 35], but, to the best of the authors knowledge, the AFEM ability to assess SIFs has never been put to test. To evaluate the accuracy of the benchmarked numerical methods, we make use of the same Mode I and Mode II load cases as those employed in Section 4.3 (see also, Figure 15). Material parameters and boundary conditions are kept the same and plane strain conditions are still assumed. The applied remote stress gives rise to the following SIFs: $K_I = 2802.5$ and $K_{II} = 2802.5$ in pure Mode I and pure Mode II, respectively.

To numerically estimate the stress intensity factors (SIFs) we proceed as follows: the energy release rate, $\mathcal{G}$, is computed thanks to a domain integral method and Irwin's relation[55] is employed to compute the SIFs in pure Mode I and II, denoted as $\hat{K_1}$ and $\hat{K_2}$:

$$\hat{K_i} = \sqrt{\frac{\mathcal{G} \times E}{1-\nu^2}} \text{ for } i \in \{I, II\} \tag{36}$$

The relative error in stress intensity factors (SIFs) is then computed as:

$$\eta = 100\% \times \frac{|K_i - \hat{K_i}|}{K_i} \text{ for } i \in \{I, II\} \tag{37}$$

Domain integral methods are commonly employed to assess energy release rates since they were shown to be coarse mesh accurate and more precise than contour integral methods [56]. In our study, we made use of the domain integral proposed by Needleman and co-workers [56] which reads:

$$\mathcal{G} = -\int_A \left(\sigma_{ij}\frac{\partial u_i}{\partial x_1} - W\delta_{1j}\right)\frac{\partial q_1}{\partial x_j} dA \tag{38}$$

where, δ_{ij} is the Kronecker delta function (such that $\delta_{ij} = 1$ if $i = j$ and $\delta_{ij} = 0$ if $i \neq j$), u_i is the i component of the displacement field, σ_{ij} is the (i, j) component of the stress tensor, W is the strain energy density, $\{x_1, x_2\} = \{x, y\}$ are the 2D Cartesian coordinates (see Figure 15), A is an annular region around the crack tip delimited by contours $C1$ and $C2$ and the crack lips, see Figure 24. and q_1 is a "sufficiently smooth"[56] scalar field defined over A, that is unity on $C1$ and vanishes on $C2$. In our computations, we chose $C1$ and $C2$ to be two crack tip-centered circles of radius $r_1 = 1.1$ and $r_2 = 1.4$, respectively, and q_1 to be an axisymmetrical field such that:

$$q_1(r, \theta) = q_1(r) = \begin{cases} \frac{r-r_2}{r_1-r_2} & \text{if } r_1 \leq r \leq r_2 \\ 1 & \text{if } r < r_1 \\ 0 & \text{if } r > r_2 \end{cases} \tag{39}$$

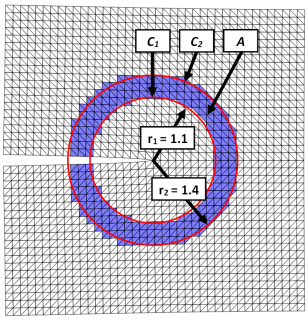

Figure 24: Surface A enclosed by contour $C1$, contour $C2$ and the crack lips, and associated finite elements

where (r, θ) are the polar coordinates associated with a reference frame centered at the crack tip (see Figure15). The evolution of the error in the stress intensity factor $K1$, under Mode I loading of the crack, is plotted in Figure 25. The SIF convergence rate is fairly independent from the employed numerical method (*i.e.*, the FEM, the AFEM or the EDM); Moes and co-workers also observed that SIFs converged with an error of $\mathcal{O}(h)$ when using the XFEM and a similar domain integral method [16]. This convergence rate is in accordance with the theoretical estimates provided by Destuynder and co-workers[57]. Despite the fact that SIFs computed with the FEM, the EDM and the AFEM converge at approximately the same rate, the FEM is noticeably less accurate than the two other methods for a given mesh size.

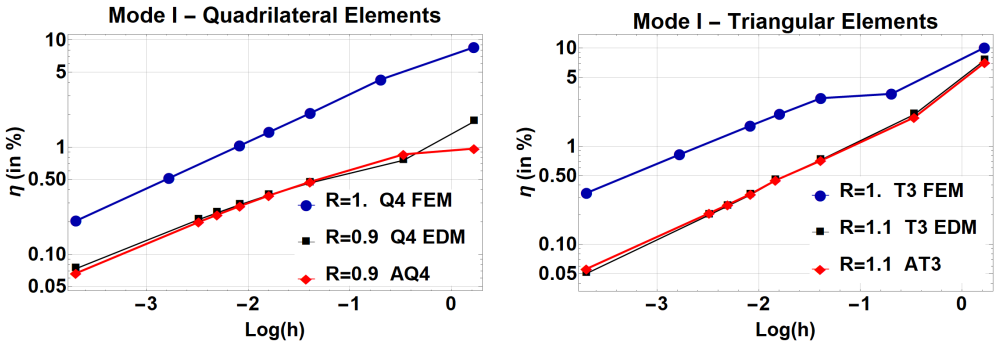

Figure 25: Mode I loading of a crack: error in the first stress intensity factor, η, as a function of the mesh size, h, and associated convergence rate, R, obtained with the finite element method (FEM), the element deletion method (EDM) and the augmented finite element method (AFEM)

By contrast, the FEM generally outperforms both the EDM and the AFEM when Mode II loading is considered, see Figure 26. One also notices that the AFEM is more accurate than the EDM in Mode II. The use of the AFEM crack-tip treatment, introduced in Section 4.3, greatly improves the AFEM solutions with coarse meshes but also degrades the SIF asymptotic convergence rate and even seems to be detrimental when fine meshes are employed. The reasons for this decrease of convergence rate have yet to be elucidated. On the whole, the results of this benchmark are similar to those related to the h-convergence in the energy norm, where the AFEM was shown to perform better than the FEM in Mode I, while being less accurate in Mode II (see Section 4.3). Thus, the underlying cause is likely to be the same: the transverse stresses at the vicinity of the crack lips, $\sigma_{xx}(x \in [0, 2.5], y = 0)$, are poorly represented

with the AFEM and makes it suboptimal, as demonstrated in Section 4.3.

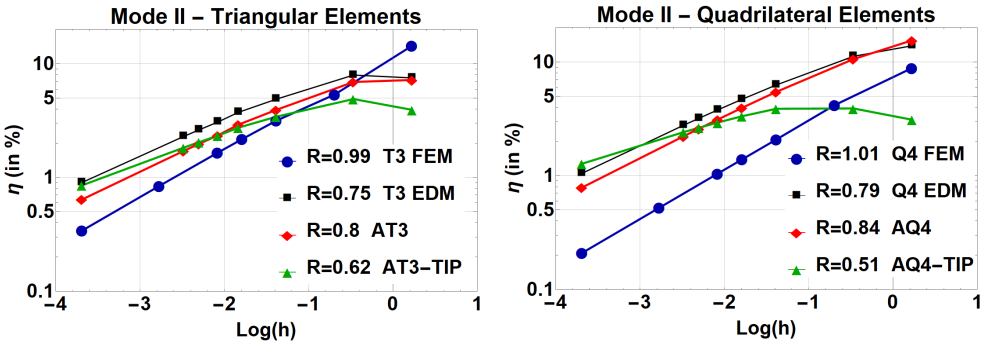

Figure 26: Mode II loading of a crack: error in the second stress intensity factor, η, as a function of the mesh size, h, and associated convergence rate, R, obtained with the FEM, the EDM, the AFEM and the AFEM with a crack-tip treatment

5. CONCLUSION

The ability of the augmented finite element method (AFEM) to model traction-free cracks has been thoroughly investigated in 2D. To make this investigation as complete as possible, triangular and quadrilateral elements were used, the ratio of element sizes between the coarsest and the finest meshes was systematically greater than 10 and errors in reaction forces, the energy norm and stress intensity factors were studied. The accuracy of the AFEM has been compared with that of the element deletion method (EDM), the finite element method (FEM), the phantom node method (PNM) and the embedded finite element method with enhanced strain modes (EFEM-SM).

The partial tension test performed in Section 4.1 allowed us to ensure that the AFEM was free from spurious stress transfer across a fully separated discontinuity. It was also discovered that, although both the EFEM-SM and the AFEM do pass the partial tension test, they give rise to noticeably different results. We demonstrated that the reaction forces and the stresses computed with the AFEM were consistent with those obtained with the standard FEM as well as with refined solutions.

The study of crack-induced stiffness loss made in Section 4.2 revealed that, under Mode I loading, the use of the AFEM, the EDM and the EFEM-SM *i*) produces virtually identical results *ii*) that outperform those obtained with the FEM and the PNM for a wide range of mesh size. By contrast, under Mode II loading, the FEM and the PNM surpass the other numerical methods. The above remarks also hold with other quantity of interests, such as the error in the energy norm (see Section 4.3) and stress intensity factors (see Section 4.4). The AFEM can be used in conjunction with a crack-tip treatment that was generally shown to improve its performance under Mode II loading. To be more precise, the crack-tip treatment systematically decreased the AFEM energy error and improved its coarse mesh accuracy when computing stress intensity factors. Despite these enhancements, the crack-tip treatment is not enough to make the AFEM solutions as accurate as the FEM ones under Mode II loading of a crack. This Mode II underperformance was found to be caused by inter-element discontinuities that locally induce an overly soft behaviour, which has a detrimental effect when crack lips are submitted to transverse stresses. A similar lack of stiffness had already been observed when using the AFEM to model weak discontinuities [53].

One goal of the current study was to determine wether the AFEM was accurate enough to be employed in analysis involving cracks. Our results demonstrated the superior accuracy of the AFEM over well-accepted methods, such as the FEM or the PNM, under Mode I loading of a crack. Yet, this is no longer the case if Mode II loading is considered. ~~However,~~Carpinteri and co-workers performed a series of cracking experiments involving double-edge notched specimens made of concrete and showed that, in this particular case, the energy dissipated through crack propagation was primarily ascribed to the Mode I fracture energy, even for mixed-mode crack propagation[58]. Moreover, well-established criteria such as the principle of local symmetry[59] state that cracks propagate in the direction that engenders a pure Mode I loading. Hence, ~~our numerical experiments prove that the AFEM can be reliably employed to assess structural failure scenarios~~ the superior Mode I accuracy of the AFEM makes it a promising method to assess structural failure scenarios. Yet, additional tests involving curved cracks or heterogeneous materials would be required to definitely ensure that a traction-free AFEM delivers reliable results in these situations.

The findings of this study also suggest that the AFEM realizes an optimal compromise between accuracy, flexibility and implementation complexity. Indeed, it performs noticeably better than the EDM in Mode II and, unlike the latter, gives access to crack openings and allows to model contact and friction between the crack lips. The accuracy of the FEM and the AFEM is on par, but the latter enjoys the same flexibility as the PNM (or the extended finite element method) in modelling cracks independently of the mesh. Moreover, a great advantage of the AFEM over methods such as the PNM is that it permits to represent an arbitrary number of cracks without increasing the number of degrees of freedom per element, or the size of the assembled stiffness matrix. Finally, the AFEM formulation is straightforward since it does not make use of enhanced strain modes, it is thus easier to implement than other EFEMs such as the EFEM-SM.

Our study focused on traction-free cracks and, as a result, does not allow to rigorously estimate the performance of the AFEM in situations where (frictional) contact between the crack lips or/and cohesive crack growth are modelled. Although the AFEM has already been successfully employed in cohesive crack propagation[18, 19, 21], it is believed that these aspects deserve further investigations geared towards assessing the convergence rate of the AFEM in such situations.

This research did not receive any specific grant from funding agencies in the public, commercial, or not-for-profit sectors.

Appendix A. Closed-form expression of the stiffness of a bilinear quadrilateral finite element submitted to partial tension

In this appendix, we derive a closed-form expression of the stiffness of the lower subdomain for the element partial test described in Section 4.1. To do so, the lower subdomain, Ω^-, is discretized with a bilinear quadrilateral element (Q4) and one seeks the analytical expression of the horizontal reaction force at node 2, $fx2$, as a function of the imposed displacement, δ, see Figure A.27. To obtain it, we first make use of the exact expressions of the Q4 stiffness matrix provided by Hacker and Schreyer[60]. The sought reaction force is then derived thanks to the method of reduction[52]. Let $\left[K^*\right]$ be the exact stiffness matrix of the aforesaid Q4, with the associated degrees of freedom, $\{q^*\}$, ordered the

following way:

$$\{q^*\} = \{u1, u2, u3, u4, v1, v2, v3, v4\}^\top \tag{A.1}$$

$\left[K^*\right]$ is split into four 4×4 submatrices:

$$\left[K^*\right] = \begin{bmatrix} K^*_{aa} & K^*_{ab} \\ K^{*\top}_{ab} & K^*_{bb} \end{bmatrix} \tag{A.2}$$

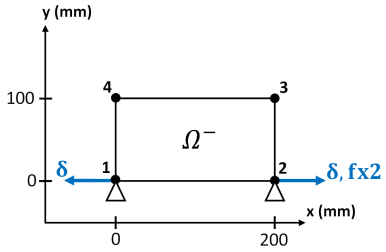

Figure A.27: Displacement boundary conditions imposed on the Q4 that modelling the lower subdomain in the partial tension test

The introduced submatrices read:

$$K^*_{aa} = \begin{pmatrix} \mathrm{B1} & \mathrm{B2} & -\frac{\mathrm{B1}}{2} & \mathrm{B3} \\ \mathrm{B2} & \mathrm{B1} & \mathrm{B3} & -\frac{\mathrm{B1}}{2} \\ -\frac{\mathrm{B1}}{2} & \mathrm{B3} & \mathrm{B1} & \mathrm{B2} \\ \mathrm{B3} & -\frac{\mathrm{B1}}{2} & \mathrm{B2} & \mathrm{B1} \end{pmatrix} \quad K^*_{bb} = \begin{pmatrix} \mathrm{B4} & \mathrm{B5} & -\frac{\mathrm{B4}}{2} & \mathrm{B6} \\ \mathrm{B5} & \mathrm{B4} & \mathrm{B6} & -\frac{\mathrm{B4}}{2} \\ -\frac{\mathrm{B4}}{2} & \mathrm{B6} & \mathrm{B4} & \mathrm{B5} \\ \mathrm{B6} & -\frac{\mathrm{B4}}{2} & \mathrm{B5} & \mathrm{B4} \end{pmatrix} \quad K^*_{ab} = \begin{pmatrix} \mathrm{B7} & \mathrm{B8} & -\mathrm{B7} & -\mathrm{B8} \\ -\mathrm{B8} & -\mathrm{B7} & \mathrm{B8} & \mathrm{B7} \\ -\mathrm{B7} & -\mathrm{B8} & \mathrm{B7} & \mathrm{B8} \\ \mathrm{B8} & \mathrm{B7} & -\mathrm{B8} & -\mathrm{B7} \end{pmatrix} \tag{A.3}$$

Under the assumption of a plane stress state, if the material is isotropic with a Young's modulus, E, and a Poisson's ratio, ν, the closed-form expressions of B1 to B8, for the Q4 represented in Figure A.27, are:

$$B1 = \frac{\mathrm{E}(2\nu - 3)}{6\,(\nu^2 - 1)} \qquad B2 = \frac{\mathrm{E}\nu}{6\,(\nu^2 - 1)} \tag{A.4}$$

$$B3 = \frac{\mathrm{E}(3 - 4\nu)}{12\,(\nu^2 - 1)} \qquad B4 = \frac{\mathrm{E}(\nu - 9)}{12\,(\nu^2 - 1)} \tag{A.5}$$

$$B5 = -\frac{\mathrm{E}(\nu + 3)}{12\,(\nu^2 - 1)} \qquad B6 = \frac{\mathrm{E}(\nu + 15)}{24\,(\nu^2 - 1)} \tag{A.6}$$

$$B7 = \frac{\mathrm{E}}{8 - 8\nu} \qquad B8 = \frac{\mathrm{E} - 3\mathrm{E}\nu}{8\,(\nu^2 - 1)} \tag{A.7}$$

To compute the sought reaction forces, the stiffness matrix $\left[K^*\right]$ is re-ordered and the resulting matrix, denoted as $\left[K\right]$, is partitioned into blocks related to known and unknown degrees of freedom. The unknown and known degrees of freedom are denoted as $\{q1\}$ and $\{q2\}$, respectively. The associated known and unknow external forces vectors are

denoted as $\{f1\}$ and $\{f2\}$, respectively. For the test case represented in Figure A.27, one has:

$$\{q1\} = \{u3, v3, u4, v4\}^\top \tag{A.8}$$

$$\{q2\} = \{u1, v1, u2, v2\}^\top = \{-\delta, 0, \delta, 0\}^\top \tag{A.9}$$

$$\{f1\} = \{fx3, fy3, fx4, fy4\}^\top = \{0, 0, 0, 0\}^\top \tag{A.10}$$

$$\{f2\} = \{fx1, fy1, fx2, fy2\}^\top \tag{A.11}$$

$$\tag{A.12}$$

With the above notations, the discretized equilibrium equation of the Q4 reads:

$$\begin{Bmatrix} f1 \\ f2 \end{Bmatrix} = \Big[K\Big] \begin{Bmatrix} q1 \\ q2 \end{Bmatrix} = \begin{bmatrix} K_{11} & K_{12} \\ K_{12}^\top & K_{22} \end{bmatrix} \begin{Bmatrix} q1 \\ q2 \end{Bmatrix} \tag{A.13}$$

All the unknowns can be obtained in two steps, one first solves for $\{q1\}$:

$$\Big\{q1\Big\} = -\Big[K_{11}\Big]^{-1}\Big[K_{12}\Big]\Big\{q2\Big\} = \begin{Bmatrix} u3 \\ v3 \\ u4 \\ v4 \end{Bmatrix} = \begin{Bmatrix} \frac{\delta(2-3\nu)\nu}{\nu(3\nu+2)-6} \\ \frac{\delta\nu(3\nu-2)}{\nu(3\nu+2)-6} \\ \frac{\delta(3-2\nu)\nu}{\nu(3\nu+2)-6} \\ \frac{\delta(3-2\nu)\nu}{\nu(3\nu+2)-6} \end{Bmatrix} \tag{A.14}$$

The unknown reaction forces, $\{f2\}$, are then readily computed:

$$\Big\{f2\Big\} = \Big[K_{12}\Big]^\top\Big\{q1\Big\} + \Big[K_{22}\Big]\Big\{q2\Big\} \tag{A.15}$$

The sought reaction forces are:

$$-fx1 = fx2 = \frac{\delta E(\nu(3\nu+2)-6)}{12\,(\nu^2-1)} \tag{A.16}$$

The material properties employed in the partial tension test of Section 4.1 are: $E = 30GPa$ and $\nu = 0$. The stiffness of the subdomain Ω^- in this case is:

$$fx2/\delta = 15kN/mm \tag{A.17}$$

References

[1] A. Combescure, A. Gravouil, D. Grégoire, J. Réthoré, X-FEM a good candidate for energy conservation in simulation of brittle dynamic crack propagation, Computer Methods in Applied Mechanics and Engineering 197 (5) (2008) 309–318. doi:10.1016/j.cma.2007.04.011.
URL http://linkinghub.elsevier.com/retrieve/pii/S0045782507001636

[2] S. Bordas, B. Moran, Enriched finite elements and level sets for damage tolerance assessment of complex structures, Engineering Fracture Mechanics 73 (9) (2006) 1176–1201. doi:10.1016/j.engfracmech.2006.01.006.
URL http://linkinghub.elsevier.com/retrieve/pii/S0013794406000257

[3] J.-Y. Wu, Unified analysis of enriched finite elements for modeling cohesive cracks, Computer Methods in Applied Mechanics and Engineering 200 (45-46) (2011) 3031–3050. doi:10.1016/j.cma.2011.05.008.
URL http://linkinghub.elsevier.com/retrieve/pii/S0045782511001812

[4] N. Moës, J. Dolbow, T. Belytschko, A finite element method for crack growth without remeshing, International Journal for Numerical Methods in Engineering 46 (1) (1999) 131–150. doi:10.1002/(SICI)1097-0207(19990910)46:1<131::AID-NME726>3.0.CO;2-J.
URL http://onlinelibrary.wiley.com/doi/10.1002/(SICI)1097-0207(19990910)46:1<131::AID-NME726>3.0.CO;2-J/abstract

[5] I. B. C. A.M. Duarte, Generalized Finite Element Methods for Three Dimensional Structural Mechanics Problems, Computers & Structures 77 (2) (2000) 215–232. doi:10.1016/S0045-7949(99)00211-4.

[6] A. Hansbo, P. Hansbo, A finite element method for the simulation of strong and weak discontinuities in solid mechanics, Computer Methods in Applied Mechanics and Engineering 193 (33-35) (2004) 3523–3540. doi:10.1016/j.cma.2003.12.041.
URL http://linkinghub.elsevier.com/retrieve/pii/S0045782504000507

[7] E. Burman, S. Claus, P. Hansbo, M. G. Larson, A. Massing, CutFEM: Discretizing geometry and partial differential equations: DISCRETIZING GEOMETRY AND PARTIAL DIFFERENTIAL EQUATIONS, International Journal for Numerical Methods in Engineering 104 (7) (2015) 472–501. doi:10.1002/nme.4823.
URL http://doi.wiley.com/10.1002/nme.4823

[8] M. Jirásek, Comparative study on finite elements with embedded discontinuities, Computer methods in applied mechanics and engineering 188 (1) (2000) 307–330.
URL http://www.sciencedirect.com/science/article/pii/S0045782599001541

[9] J. Oliver, A. Huespe, P. Sánchez, A comparative study on finite elements for capturing strong discontinuities: E-FEM vs X-FEM, Computer Methods in Applied Mechanics and Engineering 195 (37-40) (2006) 4732–4752. doi:10.1016/j.cma.2005.09.020.
URL http://linkinghub.elsevier.com/retrieve/pii/S0045782505005049

[10] E. Haghighat, S. Pietruszczak, On modeling of fractured media using an enhanced embedded discontinuity approach, Extreme Mechanics Letters 6 (2016) 10–22. doi:10.1016/j.eml.2015.11.001.
URL http://linkinghub.elsevier.com/retrieve/pii/S2352431615001224

[11] J. Oliver, I. Dias, A. Huespe, Crack-path field and strain-injection techniques in computational modeling of propagating material failure, Computer Methods in Applied Mechanics and Engineering 274 (2014) 289–348. doi:10.1016/j.cma.2014.01.008.
URL http://linkinghub.elsevier.com/retrieve/pii/S0045782514000139

[12] Y. Zhang, R. Lackner, M. Zeiml, H. A. Mang, Strong discontinuity embedded approach with standard SOS formulation: Element formulation, energy-based crack-tracking strategy, and validations, Computer Methods in Applied Mechanics and Engineering 287 (2015) 335–366. doi:10.1016/j.cma.2015.02.001.
URL http://linkinghub.elsevier.com/retrieve/pii/S0045782515000390

[13] O. Lloberas-Valls, A. Huespe, J. Oliver, I. Dias, Strain injection techniques in dynamic fracture modeling, Computer Methods in Applied Mechanics and Engineering 308 (2016) 499–534. doi:10.1016/j.cma.2016.05.023.
URL http://linkinghub.elsevier.com/retrieve/pii/S0045782516304248

[14] J.-F. Hiller, K.-J. Bathe, Measuring convergence of mixed finite element discretizations: an application to shell structures, Computers & Structures 81 (8-11) (2003) 639–654. doi:10.1016/S0045-7949(03)00010-5.
URL http://linkinghub.elsevier.com/retrieve/pii/S0045794903000105

[15] I. Babuška, J. M. Melenk, The Partition of Unity Method, International Journal for Numerical Methods in Engineering 40 (4) (1997) 727–758. doi:10.1002/(SICI)1097-0207(19970228)40:4<727::AID-NME86>3.0.CO;2-N.
URL http://onlinelibrary.wiley.com/doi/10.1002/(SICI)1097-0207(19970228)40:4<727::AID-NME86>3.0.CO;2-N/abstract

[16] E. Béchet, H. Minnebo, N. Moës, B. Burgardt, Improved implementation and robustness study of the X-FEM for stress analysis around cracks, International Journal for Numerical Methods in Engineering 64 (8) (2005) 1033–1056. doi:10.1002/nme.1386.
URL http://doi.wiley.com/10.1002/nme.1386

[17] P. Laborde, J. Pommier, Y. Renard, M. Salaün, High-order extended finite element method for cracked domains, International Journal for Numerical Methods in Engineering 64 (3) (2005) 354–381. doi:10.1002/nme.1370.
URL http://doi.wiley.com/10.1002/nme.1370

[18] W. Liu, Q. D. Yang, S. Mohammadizadeh, X. Y. Su, D. S. Ling, An accurate and efficient augmented finite element method for arbitrary crack interactions, Journal of Applied Mechanics 80 (4) (2013) 041033.

[19] W. Liu, Q. Yang, S. Mohammadizadeh, X. Su, An efficient augmented finite element method for arbitrary cracking and crack interaction in solids: EFFICIENT A-FEM FOR ARBITRARY CRACKING AND CRACK INTERACTION IN SOLIDS, International Journal for Numerical Methods in Engineering 99 (6) (2014) 438–468. doi:10.1002/nme.4697.
URL http://doi.wiley.com/10.1002/nme.4697

[20] W. Liu, D. Schesser, Q. Yang, D. Ling, A consistency-check based algorithm for element condensation in augmented finite element methods for fracture analysis, Engineering Fracture Mechanics 139 (2015) 78–97. doi:10.1016/j.engfracmech.2015.03.038.
URL http://linkinghub.elsevier.com/retrieve/pii/S0013794415001265

[21] J. Jung, B. C. Do, Q. D. Yang, Augmented finite-element method for arbitrary cracking and crack interaction in solids under thermo-mechanical loadings, Philosophical Transactions of the Royal Society A: Mathematical, Physical and Engineering Sciences 374 (2071) (2016) 20150282. doi:10.1098/rsta.2015.0282.
URL http://rsta.royalsocietypublishing.org/lookup/doi/10.1098/rsta.2015.0282

[22] Y. C. Gu, J. Jung, Q. D. Yang, W. Q. Chen, An inertia-based stabilizing method for quasi-static simulation of unstable crack initiation and propagation, Journal of Applied Mechanics 82 (10) (2015) 101010.

[23] M. Naderi, N. Apetre, N. Iyyer, Effect of interface properties on transverse tensile response of fiber-reinforced composites: Three-dimensional micromechanical modeling, Journal of Composite Materials 51 (21) (2017) 2963–2977. doi:10.1177/0021998316681189.
URL http://journals.sagepub.com/doi/10.1177/0021998316681189

[24] L. Wang, X. Ma, Q. Yang, R. L. Karkkainen, Nonlinear augmented finite element method for arbitrary cracking in large deformation plates and shells, International Journal for Numerical Methods in Engineering (2020) nme.6445doi:10.1002/nme.6445.
URL https://onlinelibrary.wiley.com/doi/abs/10.1002/nme.6445

[25] J. C. Simo, J. Oliver, F. Armero, An analysis of strong discontinuities induced by strain-softening in rate-independent inelastic solids, Computational mechanics 12 (5) (1993) 277–296.
URL http://link.springer.com/article/10.1007/BF00372173

[26] L. Cedolin, Z. P. Bažant, Effect of finite element choice in blunt crack band analysis, Computer Methods in Applied Mechanics and Engineering 24 (3) (1980) 305–316. doi:10.1016/0045-7825(80)90067-5.
URL https://linkinghub.elsevier.com/retrieve/pii/0045782580900675

[27] J. A. Zukas, Introduction to hydrocodes, Elsevier, Amsterdam; Boston, 2004.

[28] A. Pandolfi, M. Ortiz, An eigenerosion approach to brittle fracture: AN EIGENEROSION APPROACH TO BRITTLE FRACTURE, International Journal for Numerical Methods in Engineering 92 (8) (2012) 694–714. doi:10.1002/nme.4352.
URL http://doi.wiley.com/10.1002/nme.4352

[29] J.-H. Song, P. M. A. Areias, T. Belytschko, A method for dynamic crack and shear band propagation with phantom nodes, International Journal for Numerical Methods in Engineering 67 (6) (2006) 868–893. doi:10.1002/nme.1652.
URL http://doi.wiley.com/10.1002/nme.1652

[30] J. Li, E. Martin, D. Leguillon, C. Dupin, A finite fracture model for the analysis of multi-cracking in woven ceramic matrix composites, Composites Part B: Engineering 139 (2018) 75–83. doi:10.1016/j.compositesb.2017.11.050.
URL https://linkinghub.elsevier.com/retrieve/pii/S1359836817306777

[31] T. J. R. Hughes, The finite element method: linear static and dynamic finite element analysis, Prentice-Hall, Englewood Cliffs, N.J, 1987.

[32] O. C. Zienkiewicz, R. L. Taylor, J. Zhu, The finite element method. Vol. 1: Its basis and fundamentals, 6th Edition, Elsevier Butterworth-Heinemann, Amsterdam, 2010.

[33] K.-J. Bathe, Finite element procedures, 2nd Edition, Prentice-Hall, Englewood Cliffs, N.J, 2014.

[34] A. R. Ingraffea, R. de Borst, Computational Fracture Mechanics, in: E. Stein, R. de Borst, T. J. R. Hughes (Eds.), Encyclopedia of Computational Mechanics Second Edition, John Wiley & Sons, Ltd, Chichester, UK, 2017, pp.

1–26. doi:10.1002/9781119176817.ecm2032.
URL http://doi.wiley.com/10.1002/9781119176817.ecm2032

[35] R. Branco, F. Antunes, J. Costa, A review on 3D-FE adaptive remeshing techniques for crack growth modelling, Engineering Fracture Mechanics 141 (2015) 170–195. doi:10.1016/j.engfracmech.2015.05.023.
URL https://linkinghub.elsevier.com/retrieve/pii/S0013794415002209

[36] T. Pin, T. H. Pian, On the convergence of the finite element method for problems with singularity, International Journal of Solids and Structures 9 (3) (1973) 313–321. doi:10.1016/0020-7683(73)90082-6.
URL https://linkinghub.elsevier.com/retrieve/pii/0020768373900826

[37] R. S. Barsoum, On the use of isoparametric finite elements in linear fracture mechanics, International Journal for Numerical Methods in Engineering 10 (1) (1976) 25–37. doi:10.1002/nme.1620100103.
URL http://doi.wiley.com/10.1002/nme.1620100103

[38] J.-H. Song, P. M. A. Areias, T. Belytschko, A method for dynamic crack and shear band propagation with phantom nodes, International Journal for Numerical Methods in Engineering 67 (6) (2006) 868–893. doi:10.1002/nme.1652.
URL http://doi.wiley.com/10.1002/nme.1652

[39] N. Vu-Bac, H. Nguyen-Xuan, L. Chen, C. K. Lee, G. Zi, X. Zhuang, G. R. Liu, T. Rabczuk, A Phantom-Node Method with Edge-Based Strain Smoothing for Linear Elastic Fracture Mechanics, Journal of Applied Mathematics 2013 (2013) 1–12. doi:10.1155/2013/978026.
URL http://www.hindawi.com/journals/jam/2013/978026/

[40] E. N. Dvorkin, A. M. Cuitiño, G. Gioia, Finite elements with displacement interpolated embedded localization lines insensitive to mesh size and distortions, International journal for numerical methods in engineering 30 (3) (1990) 541–564.
URL http://onlinelibrary.wiley.com/doi/10.1002/nme.1620300311/full

[41] M. Jirasek, T. Zimmermann, Embedded crack model. Part II: Combination with smeared cracks, International Journal for Numerical Methods in Engineering 50 (6) (2001) 1291–1305.

[42] M. Jirásek, T. Belytschko, Computational resolution of strong discontinuities, in: Proceedings of fifth world congress on computational mechanics, WCCM V, Vienna University of Technology, Austria, 2002.

[43] D. Ehrlich, F. Armero, Finite element methods for the analysis of softening plastic hinges in beams and frames, Computational Mechanics 35 (4) (2005) 237–264. doi:10.1007/s00466-004-0575-z.
URL http://link.springer.com/10.1007/s00466-004-0575-z

[44] O. Manzoli, P. Shing, A general technique to embed non-uniform discontinuities into standard solid finite elements, Computers & Structures 84 (10-11) (2006) 742–757. doi:10.1016/j.compstruc.2005.10.009.
URL http://linkinghub.elsevier.com/retrieve/pii/S0045794905003871

[45] C. Linder, F. Armero, Finite elements with embedded strong discontinuities for the modeling of failure in solids, International Journal for Numerical Methods in Engineering 72 (12) (2007) 1391–1433. doi:10.1002/nme.2042.
URL http://doi.wiley.com/10.1002/nme.2042

[46] J. Dujc, B. Brank, A. Ibrahimbegovic, Stress-hybrid quadrilateral finite element with embedded strong discontinuity for failure analysis of plane stress solids: STRESS-HYBRID QUADRILATERAL WITH EMBEDDED DISCONTINUITY, International Journal for Numerical Methods in Engineering 94 (12) (2013) 1075–1098. doi:10.1002/nme.4475.
URL http://doi.wiley.com/10.1002/nme.4475

[47] F. Armero, J. Kim, Three-dimensional finite elements with embedded strong discontinuities to model material failure in the infinitesimal range: 3D FINITE ELEMENTS WITH EMBEDDED STRONG DISCONTINUITIES, International Journal for Numerical Methods in Engineering 91 (12) (2012) 1291–1330. doi:10.1002/nme.4314.
URL http://doi.wiley.com/10.1002/nme.4314

[48] C. Linder, X. Zhang, A marching cubes based failure surface propagation concept for three-dimensional finite elements with non-planar embedded strong discontinuities of higher-order kinematics: A MARCHING CUBES-BASED FAILURE SURFACE PROPAGATION CONCEPT, International Journal for Numerical Methods in Engineering 96 (6) (2013) 339–372. doi:10.1002/nme.4546.
URL http://doi.wiley.com/10.1002/nme.4546

[49] P. Prabhakar, A. M. Waas, A novel continuum-decohesive finite element for modeling in-plane fracture in fiber reinforced composites, Composites Science and Technology 83 (2013) 1–10. doi:10.1016/j.compscitech.2013.03.022.
URL https://linkinghub.elsevier.com/retrieve/pii/S0266353813001450

[50] X. Li, J. Chen, The implementation of the extended cohesive damage model for multicrack evolution in laminated composites, Composite Structures 139 (2016) 68–76. doi:10.1016/j.compstruct.2015.11.080.
URL https://linkinghub.elsevier.com/retrieve/pii/S0263822315010971

[51] N. Sukumar, A. Tabarraei, Conforming polygonal finite elements, International Journal for Numerical Methods in Engineering 61 (12) (2004) 2045–2066. doi:10.1002/nme.1141.
URL http://doi.wiley.com/10.1002/nme.1141

[52] B. Wu, Z. Xu, Z. Li, A note on imposing displacement boundary conditions in finite element analysis, Communications in Numerical Methods in Engineering 24 (9) (2007) 777–784. doi:10.1002/cnm.989.
URL http://doi.wiley.com/10.1002/cnm.989

[53] S. Essongue, G. Couégnat, E. Martin, Performance assessment of the augmented finite element method for the modeling of weak discontinuities, International Journal for Numerical Methods in Engineering (2020) nme.6530doi:10.1002/nme.6530.
URL https://onlinelibrary.wiley.com/doi/10.1002/nme.6530

[54] H. M. Westergaard, Bearing pressures and cracks, J. App. Mechanics 6 (1) (1939) 49–53.

[55] G. R. Irwin, Analysis of stresses and strains near the end of a crack traversing a plate, Journal of Applied Mechanics 24 (1957) 361–364.

[56] F. Li, C. Shih, A. Needleman, A comparison of methods for calculating energy release rates, Engineering Fracture Mechanics 21 (2) (1985) 405–421. doi:10.1016/0013-7944(85)90029-3.
URL https://linkinghub.elsevier.com/retrieve/pii/0013794485900293

[57] P. Destuynder, M. Djaoua, S. Lescure, Some remarks on elastic fracture mechanics, Journal de Mécanique Théorique et Appliquée 2 (1983) 113–135.

[58] A. Carpinteri, S. Valente, G. Ferrara, G. Melchiorrl, Is mode II fracture energy a real material property?, Computers & Structures 48 (3) (1993) 397–413. doi:10.1016/0045-7949(93)90316-6.
URL https://linkinghub.elsevier.com/retrieve/pii/0045794993903166

[59] R. V. Gol'dstein, R. L. Salganik, Brittle fracture of solids with arbitrary cracks, International Journal of Fracture 10 (4) (1974) 507–523. doi:10.1007/BF00155254.
URL http://link.springer.com/10.1007/BF00155254

[60] W. L. Hacker, H. L. Schreyer, Eigenvalue analysis of compatible and incompatible rectangular four-node quadrilateral elements, International Journal for Numerical Methods in Engineering 28 (3) (1989) 687–703. doi:10.1002/nme.1620280315.
URL http://doi.wiley.com/10.1002/nme.1620280315

Highlights:

- The convergence rate of the AFEM is numerically evaluated
- The singularity of AFEM stiffness matrices is dealt with
- The accuracy of the AFEM is thoroughly benchmarked against popular numerical methods
- The AFEM outperforms the other evaluated methods under Mode I loading of a crack

Declaration of interests

☒ The authors declare that they have no known competing financial interests or personal relationships that could have appeared to influence the work reported in this paper.

☐The authors declare the following financial interests/personal relationships which may be considered as potential competing interests: